Lysosomal proteomics reveals mechanisms of neuronal apoE4-associated lysosomal dysfunction

Authors

Einar K. Krogsaeter,[a,b,c,n] Justin McKetney,[a,b,c,n] Leopoldo Valiente-Banuet,[d] Angelica Marquez,[a,b,c] Alexandra Willis,[a,b,c] Zeynep Cakir,[a,b,c] Erica Stevenson,[a,b,c] Gwendolyn M. Jang,[a,b,c] Antara Rao,[e,f] Emmy Li,[g,h] Anton Zhou,[e] Anjani Attili,[g,i] Timothy S. Chang,[d] Martin Kampmann,[g,j] Yadong Huang,[e,f,h,k,l,m] Nevan J. Krogan,[a,b,c] Danielle L. Swaney[a,b,c,*]

Affiliations

[a]Gladstone Data Science and Biotechnology Institute, The J. David Gladstone Institutes, San Francisco, California, USA
[b]Quantitative Bioscience Institute, University of California, San Francisco, California, USA
[c]Department of Cellular and Molecular Pharmacology, University of California, San Francisco, California, USA
[d]Department of Neurology, David Geffen School of Medicine, University of California, Los Angeles, Los Angeles, California, USA
[e]Gladstone Institute of Neurological Disease, The J. David Gladstone Institutes, San Francisco, USA
[f]Developmental and Stem Cell Biology Graduate Program, University of California, San Francisco, USA
[g]Institute for Neurodegenerative Diseases, University of California, San Francisco, California, USA
[h]Biomedical Sciences Graduate Program, University of California, San Francisco, USA
[i]Biosciences Internship Program, City College of San Francisco, USA
[j]Department of Biochemistry and Biophysics, University of California, San Francisco, California, USA
[k]Neuroscience Graduate Program, University of California, San Francisco, USA
[l]Gladstone Center for Translational Advancement, Gladstone Institutes, San Francisco, USA
[m]Departments of Neurology and Pathology, University of California, San Francisco, USA
[n]These authors contributed equally
*Corresponding author. ORCID: 0000-0001-6119-6084. Email: danielle.swaney@ucsf.edu. Address: 1700 4th Street, #301, San Francisco, CA 94158, USA.

Keywords

Alzheimer Disease; apoE4; Lgals3bp; LysoIP; lysosomes; pH; Tmed5

Abstract

ApoE4 is the primary risk factor for Alzheimer Disease (AD). Early AD pathological events first affect the neuronal endolysosomal system, which in turn causes neuronal protein aggregation and cell death. Despite the crucial influence of lysosomes upon AD pathophysiology, and that apoE4 localizes to lysosomes, the influence of apoE4 on lysosomal function remains unexplored. We find that expression of apoE4 in neuronal cell lines results in lysosomal alkalinization and impaired lysosomal function. To identify driving factors for these defects, we performed quantitative lysosomal proteome profiling. This revealed that apoE4 expression results in differential regulation of numerous lysosomal proteins, correlating with apoE allele status and disease severity in AD brains. In particular, apoE4 expression results in the depletion of lysosomal Lgals3bp and the accumulation of lysosomal Tmed5. We additionally validated that these lysosomal protein changes can be targeted to modulate lysosomal function. Taken together, this work thereby reveals that apoE4 causes widespread lysosomal defects through remodeling the lysosomal proteome, with the lysosomal Tmed5 accumulation and Lgals3bp depletion manifesting as lysosomal alkalinization in apoE4 neurons.

Abbreviations

Aβ	β-Amyloid
AD	Alzheimer Disease
APMS	Affinity purification mass spectrometry
apoE	Apolipoprotein E
App	Amyloid precursor protein
BafA1	Bafilomycin A1
CMA	Chaperone-mediated autophagy
COP	Coatomer
ER	Endoplasmic reticulum
ERAD	Endoplasmic reticulum-associated degradation
ERGIC	Endoplasmic reticulum-Golgi intermediate compartment
FCCP	Carbonyl cyanide p-trifluoro methoxyphenylhydrazone
GABA	Gamma-aminobutyric acid
GFP	Green fluorescent protein
GPI	Glycerophosphoinositol
GPN	Glycyl-L-phenylalanine 2-naphthylamide
HA	Hemagglutinin protein tag
iPSC	Induced pluripotent stem cells
LAMP1	Lysosome-associated membrane protein 1
Lgals3bp	Galectin 3-binding protein
LysoIP	Lysosomal immunoprecipitation
Mapt	Microtubule-associated protein tau
MR-CtsB	Magic red cathepsin B
MS	Mass spectrometry
NFT	Neurofibrillary tangles
PCA	Principal component analysis
PLA	Proximity ligation assay

PSEN1	Presenilin 1
Psen2	Presenilin 2
pTau	Phospho-tau
ROS	Reactive oxygen species
RT-qPCR	Reverse transcriptase quantitative polymerase chain reaction
SEM	Standard error of the mean
siRNA	Short interfering RNA
SRCR	Scavenger receptor cysteine-rich domain
Tau	Microtubule-associated protein tau
Tmed	Transmembrane emp24 domain-containing protein
TMEM192	Transmembrane protein 192

Introduction

Alzheimer Disease (AD) is the most common form of dementia and is expected to remain a continuing major global health burden, with cases predicted to double to more than 130 million worldwide by 2050 [1]. Although the molecular and cellular complexities of AD present significant challenges for tackling this devastating disease, the apolipoprotein (apo) E4 genetic variant stands out as a predominant feature among AD cases [2, 3]. This variant, marked by the single amino acid substitution C130R, is not only found in 60-70% percent of all sporadic and familial AD cases, but is also associated with a lower age of AD onset [4–6]. Structurally, apoE4 favors intramolecular domain interaction between its N-terminal 4-helix bundle/receptor-binding domain and the C-terminal lipid binding region, taking on a closed conformation. The closed apoE4 variant thus shifts its preference from small, phospholipid-rich HDL particles to large triglyceride-rich VLDL particles [7]. ApoE4 also modifies the disease trajectory of autosomal dominant, early-onset AD, accelerating cognitive decline in *PSEN1* E280A carriers [8]. Importantly, APOE4 carriers frequently present with two hallmark pathologies of AD: Tau neurofibrillary tangles (NFTs) and β-amyloid plaques.

Considering that APOE4 is both a strong genetic risk factor for AD and is relatively common among the general population (20-25%), significant efforts have been made to understand the mechanisms by which APOE4 drives AD biology. Specifically neuronal apoE4 appears central in AD pathogenesis: While neurons typically express a minority (~20%) of the total brain apoE [9], stress and neuronal injury results in alternative apoE splicing, facilitating its translation and increasing neuronal apoE protein production [10]. Importantly, this neuronal apoE appears central to AD pathogenesis, as its cell-type specific removal prevents both AD-associated cognitive decline [9] and hallmark AD pathology [11]. It is commonly accepted that apoE4 affects a variety of neuronal functions, reducing synaptic plasticity and density [12–15], decreasing the hippocampal volume [11, 16], and impairing learning and memory [17–21]. Importantly, these effects can be cell-type specific, with evidence for both neuronal [11, 22–25] and glial [21, 26, 27] apoE4 expression individually influencing AD related processes. At a cellular level, apoE4 interferes with cytoskeletal and microtubule structure [28–31], β-amyloid clearance [32–34], tau dynamics [11], metabolism [35–37], and endolysosomal function [15, 26, 38–41]. Several of these outcomes could

be, in part, attributed to endolysosomal defects, as lysosomes clear defective organelles and larger protein aggregates.

Conversely, loss of lysosomal proteins can result in lysosomal storage and cause AD [42–44] or similar neurodegenerative diseases [45–49]. Inhibition of lysosomal function also directly leads to development of AD pathological features such as β-amyloid accumulation [50–52]. While apoE4 has previously been shown to impair endosomal trafficking and cause the accumulation of aggregate-prone proteins such as β-amyloid [53], its influence on lysosomal activity has not been explored. Besides APOE, mutations within other genetic risk factors for AD, such as rare presenilin-1 (PSEN1) mutations associated with early-onset AD, cause lysosomal mislocalization of the γ-secretase complex, resulting in an intracellular pool of aggregation-prone Aβ42 [54]. While PSEN1 is known to directly regulate lysosomal acidification and function [55], the effect of apoE4 on lysosomal homeostasis remains incompletely explored. A recent article described how exogenously administered apoE4 preferentially traffics to late endosomes/lysosomes and impairs autophagic flux [56]. Furthermore, lysosomal alkalinization has been observed in apoE4-expressing astrocytes, although its etiology and ramifications were not studied in depth [26]. To address this knowledge gap, we hypothesized that apoE4 expression intrinsically influences lysosomal function in neurons. To investigate this, we employed apoE-expressing neuronal cell lines and iPSC-derived neurons to evaluate how apoE4 expression affects lysosomal function and discover alterations to lysosomal proteins that drive apoE4-associated lysosomal defects.

Results

ApoE4 expression dramatically abrogates lysosomal function

While it has previously been shown that apoE4 expression interferes with astrocytic autophagy [57] and lysosomal pH [26], the effects of apoE4 expression on lysosomal function in neuronal cells, as well as the consequences of such lysosomal alkalinization, are unexplored. We set out to investigate the lysosomal influence of human apoE (hAPOE) in Neuro-2a cells, a tractable model system for studying apoE4-associated neuropathology. Importantly, physiologically relevant expression levels of hAPOE (both E3 and E4 variant) were achieved by introduction of human APOE locus flanked by 5kb and 8kb of its 5' and 3' genomic regions, respectively [58]. Having verified that the Neuro-2a cells expressed similar levels of apoE on a mRNA (Fig. S1A) and protein level (previous article, see [31]), we next assessed whether apoE4 influences lysosomal acidification by labeling lysosomes in hAPOE3- and hAPOE4-expressing cells using Lysotracker. The intensity of Lysotracker staining correlates with both the number of endolysosomal vesicles and their luminal acidity. We found that the Lysotracker intensity was significantly reduced in hAPOE4-expressing cells (Fig. 1A-B), suggesting either endolysosomal alkalinization or a reduction in endolysosomal density. We therefore stained the cells for the lysosomal membrane marker LAMP1, finding that the lysosomal density was not decreased in hAPOE4 cells (Fig. S1B-C). These findings suggested that defective acidification may underly our observations.

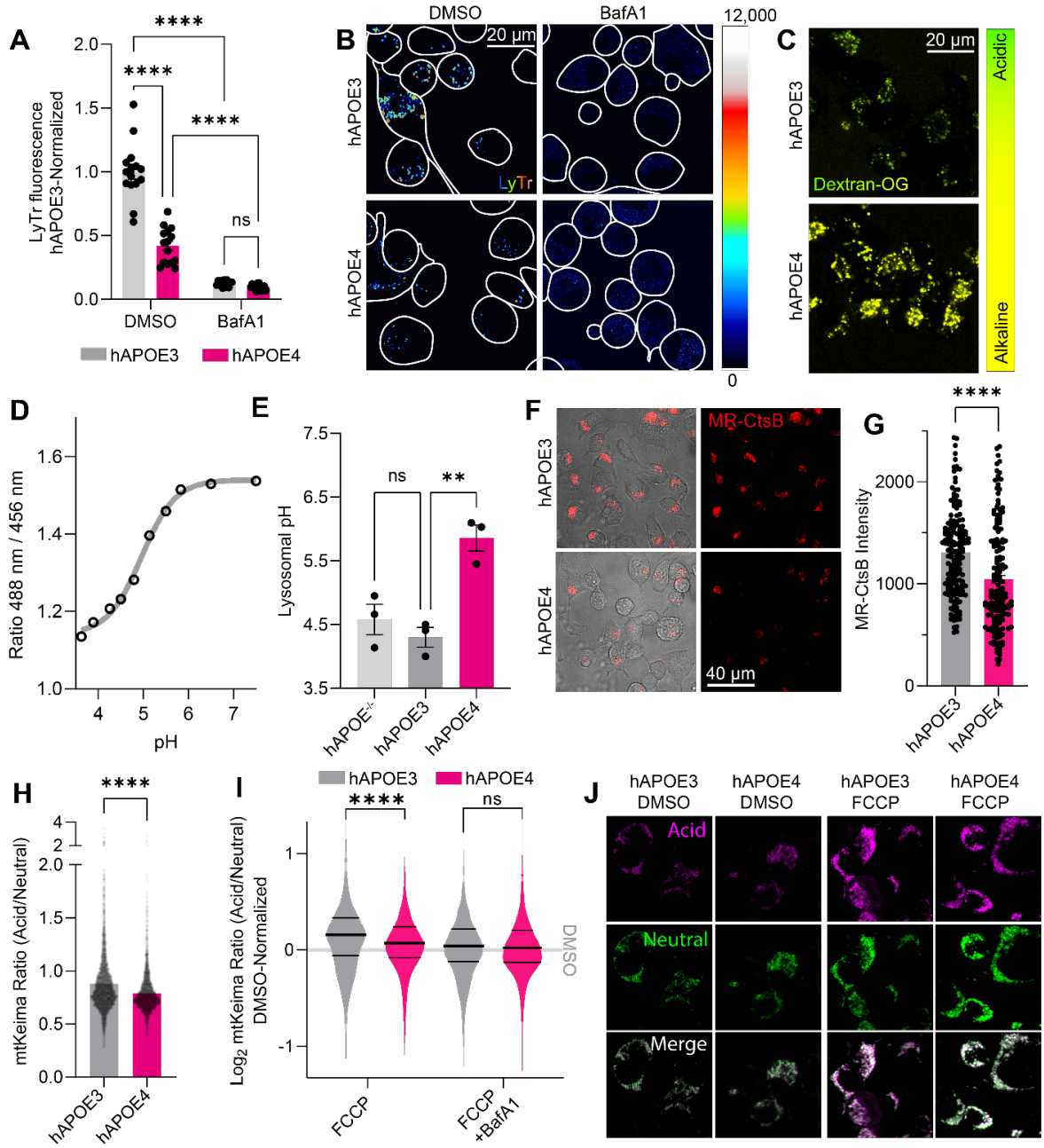

Figure 1: ApoE4 expression impairs lysosomal function. (**A**) LysoTracker Deep Red was used to stain acidic compartments of hAPOE-expressing Neuro-2a cells. Staining intensity was calculated per cell, and summarized for each image, across three independent experiments. Bafilomycin A1 was used to block lysosomal acidification, decreasing the lysotracker staining intensity. (**B**) Representative images for (A). (**C**) Images of lysosomal pH measurements in hAPOE-expressing Neuro-2a cells using OregonGreen-70,000 kDa Dextran. (**D**) Standard curve for the OregonGreen ratio to pH conversion. (**E**) Lysosomal pH values measured by OregonGreen experiments. Data points represent individual experiments. (**F**) Images of Magic Red-Cathepsin B (MR-CtsB)-stained hAPOE-expressing Neuro-2a cells, indicating lysosomal proteolysis. (**G**) MR-CtsB quantification of proteolytic cleavage, as shown in panel (F). Data points indicate individual mitochondria across three independent experiments. (**H**) Basal mtKeima measurements from hAPOE-expressing Neuro-2a cells. Data points represent individual mitochondria imaged across three independent experiments. (**I**) Log2-transformed mtKeima ratios normalized to genotype DMSO controls, following 1-hour mitophagic induction by FCCP and BafA1 to inhibit lysosomal acidification, plotted as a density plot of analyzed mitochondria across three independent experiments. Thick central line indicates the experimental mean, thinner flanking lines indicate the 1st and 3rd quartiles. (**J**) Representative images for (I). All experiments were performed as three independent technical and biological replicates, and analyzed in Fiji. The data was plotted as means with SEM error bars, and analyzed in GraphPad Prism by 2-way ANOVA followed *post-hoc* by Bonferroni's multiple comparisons test (A,E,G,I) or an unpaired, two-tailed t-test (H).**P<0.01, ****P<0.0001.

122 In order to accurately measure the lysosomal pH, we employed the OregonGreen-dextran probe to
123 ratiometrically measure the lysosomal pH. OregonGreen-dextran is routed to lysosomes by an
124 overnight pulse, followed by a chase period allowing its endosomal (but not lysosomal) efflux. We
125 next pH-clamped the lysosomes using a range of standard buffers to generate a standard curve of
126 OregonGreen intensities. We could thereby extrapolate the OregonGreen intensity ratios to absolute
127 pH values. We found that hAPOE4-expressing cells exhibit dramatic lysosomal alkalinization
128 (pH=5.86) compared to hAPOE3 (pH=4.30) cells (Fig. 1C-E), reminiscent of previous results in
129 apoE4-expressing astrocyte lysosomes (pH=5.20, compared to pH=4.08 in apoE3 astrocytes) [26].
130 This alkalinization was also observed in comparison to the parental cell line in which no human
131 APOE had been introduced (and hAPOE$^{-/-}$ (pH=4.58). In contrast, the lysosomal pH was
132 comparable between hAPOE3 and hAPOE$^{-/-}$ cells (Fig. 1E). These results suggest that hAPOE4
133 uniquely confers a toxic gain-of-function to lysosomes.

134 Maintenance of lysosomal pH is required for autophagy. We therefore assessed colocalization of
135 lysosomes with autophagosomal LC3, and measured the cellular LC3-II/LC3-I ratios as an indicator
136 for autophagic induction and flux. Autophagy appeared generally functional in these cells, despite
137 the basal autophagy being slightly dampened in hAPOE4 cells (Fig. S1D-F). Since the lysosomal
138 pH gradient is in part maintained by H^+/Ca^{2+} antiporters [59], we also examined the lysosomal Ca^{2+}
139 content. We targeted a previously described [60] genetically encoded calcium indicator to the
140 lysosomes to measure lysosomal calcium release. Using GPN to release lysosomal calcium [61],
141 we found lysosomal calcium levels to be comparable between hAPOE3 and hAPOE4-expressing
142 cells (Fig. S1G-L), particularly after correcting for lysosomal density (Fig. S1M). These findings
143 suggest that the apoE4-associated lysosomal alkalinization is distinct from lysosomal Ca^{2+} storage.
144 Lysosomes normally maintain their pH at a range between 4.00 and 5.00 to support their resident,
145 H^+-dependent proteases. Lysosomal alkalinization naturally occurs upon ageing and cellular
146 senescence, resulting in impaired lysosomal proteolysis and accumulation of protein aggregates.
147 Hypothesizing that the apoE4-associated lysosomal alkalinization also impairs lysosomal
148 degradation, we loaded the cells with Magic Red Cathepsin B (MR-CtsB), a dye that is sequestered
149 in lysosomes and fluoresces upon its cathepsin-dependent proteolytic cleavage. We found that the
150 hAPOE4-expressing cells exhibited significantly decreased MR-CtsB proteolysis compared to
151 hAPOE3-expressing cells, in line with their decreased lysosomal acidity (Fig. 1F-G). Similarly,
152 lysosomal function is crucial for the clearance of defective organelles, including mitochondrial
153 degradation through mitophagy [60]. Mitophagy can be readily measured using the mtKeima probe
154 [62]. Under basal conditions, we observed a modest impairment of mitophagy in hAPOE4 cells
155 (Fig. 1H). While FCCP triggered mitophagy in both hAPOE3- and hAPOE4-expressing cells, its
156 induction was stronger in the hAPOE3-expressing cells (Fig. 1I-J). To validate that we detected the
157 uptake of mitochondria into lysosomes, we combined FCCP treatment with bafilomycin A1
158 (BafA1) to block lysosomal acidification. While BafA1 as expected reduced the acidic mtKeima
159 signal, it intriguingly also abrogated the difference between hAPOE3- and hAPOE4-expressing
160 cells (Fig. 1I), suggesting that mitophagic defects could be attributed to defective lysosomal
161 acidification. Having established that neuronal apoE4 expression leads to widespread lysosomal
162 impairments, we set out to explore the molecular mechanisms underlying this phenomenon.

163 ***Identification of lysosomal proteins via LysoIP proteomics***

164 Since proteins serve as principal biological effectors that many be intrinsically tied to the observed
165 lysosomal impairment, we examined changes to the lysosomal proteome upon apoE4 expression.
166 We used lentiviral transduction to introduce the lysosomal tag TMEM192-3xHA into each of our
167 Neuro-2a cell lines (hAPOE$^{-/-}$, hAPOE3, and hAPOE4) [63]. Lysosomes were visualized in
168 transduced cells by immunostaining for the 3xHA tag, with no immunoreactivity in background
169 cells (Fig. 2A). We immunoprecipitated the HA-tagged lysosomes (LysoIP) to isolate the lysosomal
170 proteome, using untagged cells as a background proteome to control for non-specific binding to the
171 anti-HA beads (Fig. 2B). Additionally, to provide greater context for alterations observed in the
172 lysosomal proteome, we also measured protein abundances from whole cell lysates for each of the
173 apoE genotypes. Although all cells expressed comparable levels of TMEM192, with the protein
174 being particularly enriched in lysosomal fractions, slightly more TMEM192 was detected in
175 hAPOE3 lysosomes (Fig. S2A). Overall, the lysosomal protein entities detected, and the relative
176 frequencies of these, were comparable across genotypes (Fig. S2B-C). As expected, clustering of
177 protein abundances across all samples revealed distinct proteome signatures between the three
178 different experimental groups (whole cell lysate, LysoIP, and background), with no discernible
179 influence of overexpressing the lysosomal TMEM192-3xHA tag on the whole-cell proteome (Fig.
180 2C; full heat-maps shown in Fig. S3A-B; Table S1A). Additionally, compared to the background
181 samples, our LysoIP samples were appropriately enriched in proteins with lysosomal annotations
182 as compared to other subcellular organelles (Fig. 2D). Next, we focused on defining the lysosomal
183 proteome. First, we identified enriched lysosomal proteins by comparing the tagged and
184 background samples for each genotype. We considered proteins to be lysosomal if they were either
185 exclusively detected in LysoIP samples, or significantly enriched in LysoIP samples relative to
186 background samples (>2-fold, and $p<0.05$) (Fig. 2E; Table S1B-C). Gene set enrichment analysis
187 of these proteins highlighted an enrichment of lysosome-associated terms, including autophagy,
188 endosome membrane, late endosome, and vacuolar membrane (Fig. 2F). As expected, the most
189 significantly enriched proteins included well-known lysosomal proteins, including degradative
190 enzymes (Ctsd, Psma3), proton pump subunits (Atp6v1e1), metabolic enzymes (Gusb), and
191 lysosomal scaffold proteins (Lamtor 2/4). However, we also found a number of proteins to be
192 detected exclusively and reproducibly across all lysosomal samples, but that have not yet been
193 ascribed a lysosomal function. These include constituents of the Usp8:Ptpn23:Stam2 and
194 Nedd4:Litaf:Bmpr1 deubiquitin- and ubiquitination complexes, and the early endosome/Rab5a-
195 associated proteins Rabep1 and Rabgef1. While neither complex is appreciated to function in the
196 lysosome, their respective implicated processes of protein ubiquitination and Rab protein activation
197 could conceivably be of lysosomal importance. Lastly, the primary driver of differences between
198 LysoIP samples, as determined by principal component analysis (PCA), was found to be
199 bafilomycin treatment, (Fig. S4A), and was distinguished by lysosomal accumulation of chaperonin
200 TCP-1 subunits, proteasome subunits, and the dynein complex, alongside loss of cathepsins, the
201 GATOR2 complex, and glycosyl hydrolases (Fig. S4B; Table S1C).

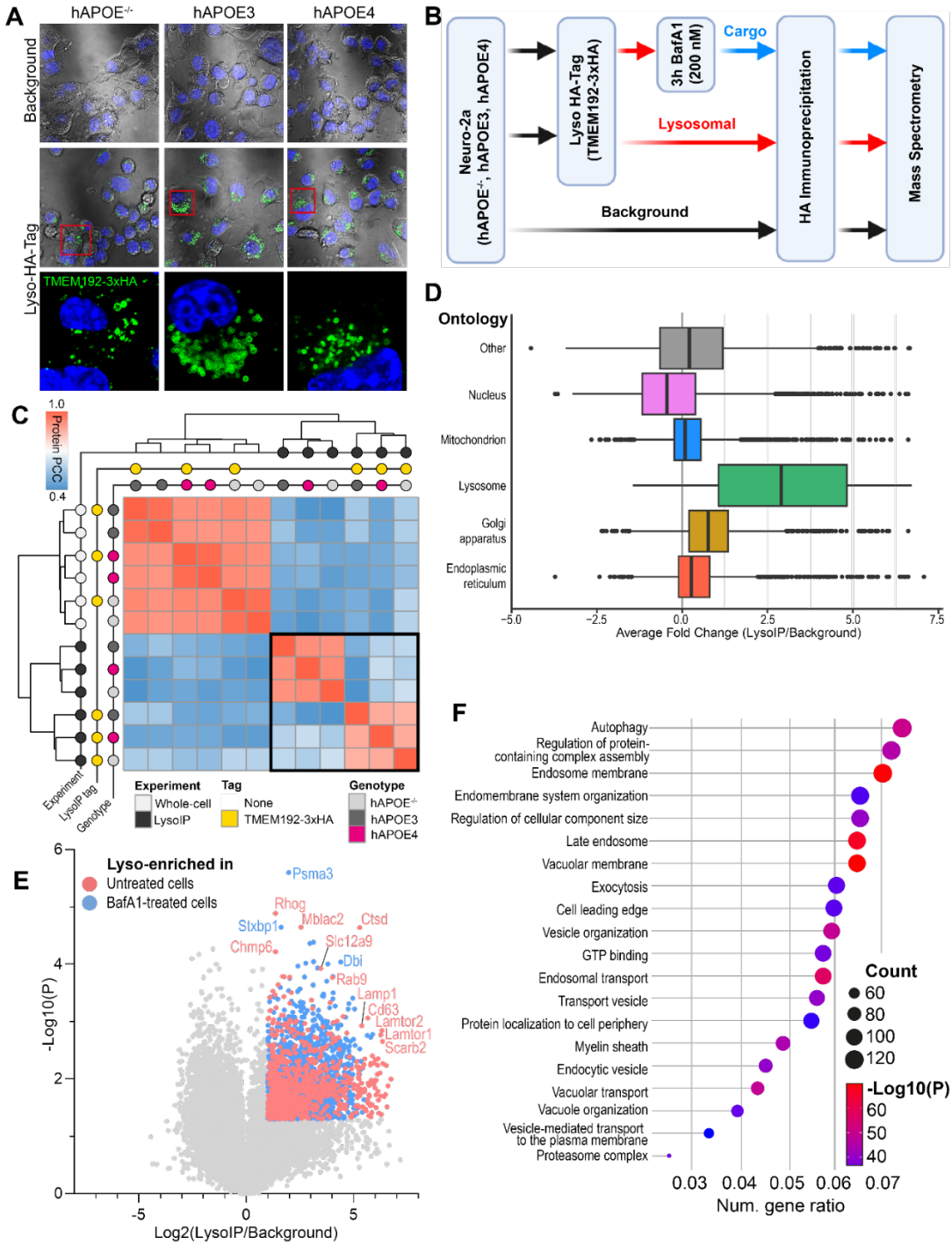

Figure 2: Isolation of lysosomes by lysosomal immunoprecipitation (LysoIP). (**A**) Immunostaining of the lysosomal TMEM192-3xHA tag shows immunoreactivity only in polyclonal, transduced Neuro-2a cells. (**B**) Schematic of the LysoIP workflow. Note, paired samples from whole cell lysates of each of these conditions were also analyzed. (**C**) Clustered heatmap of protein similarities (measured by global protein Pearson's correlation coefficient; PCC) between sample sets reveals clustering of whole-cell, LysoIP background and LysoIP-tagged samples. Sample sets within the black bounding box are further analyzed in panels (D-E). (**D**) Box plot of protein abundances in the untreated LysoIP samples relative to background IP samples. Proteins have been separated based on their subcellular compartment ontologies. (**E**) Volcano plot of untreated or Baf1A treated LysoIP samples as compared to background IP samples. Colored dots indicate proteins with the minimum enrichment (Log2(LysoIP/Background)>1 and p<0.05) to be categorized as lysosomal proteins. (**F**) Gene ontology enrichment of Neuro-2a lysosomal proteins (either exclusively detected in LysoIP samples or significantly enriched in LysoIP samples relative to background, as indicated in panel E). Dot size indicates the number of lysosomal proteins matching to that ontology term, while the color represents the enrichment of that ontology term.

Proteomic alterations to apoE4-associated lysosomes

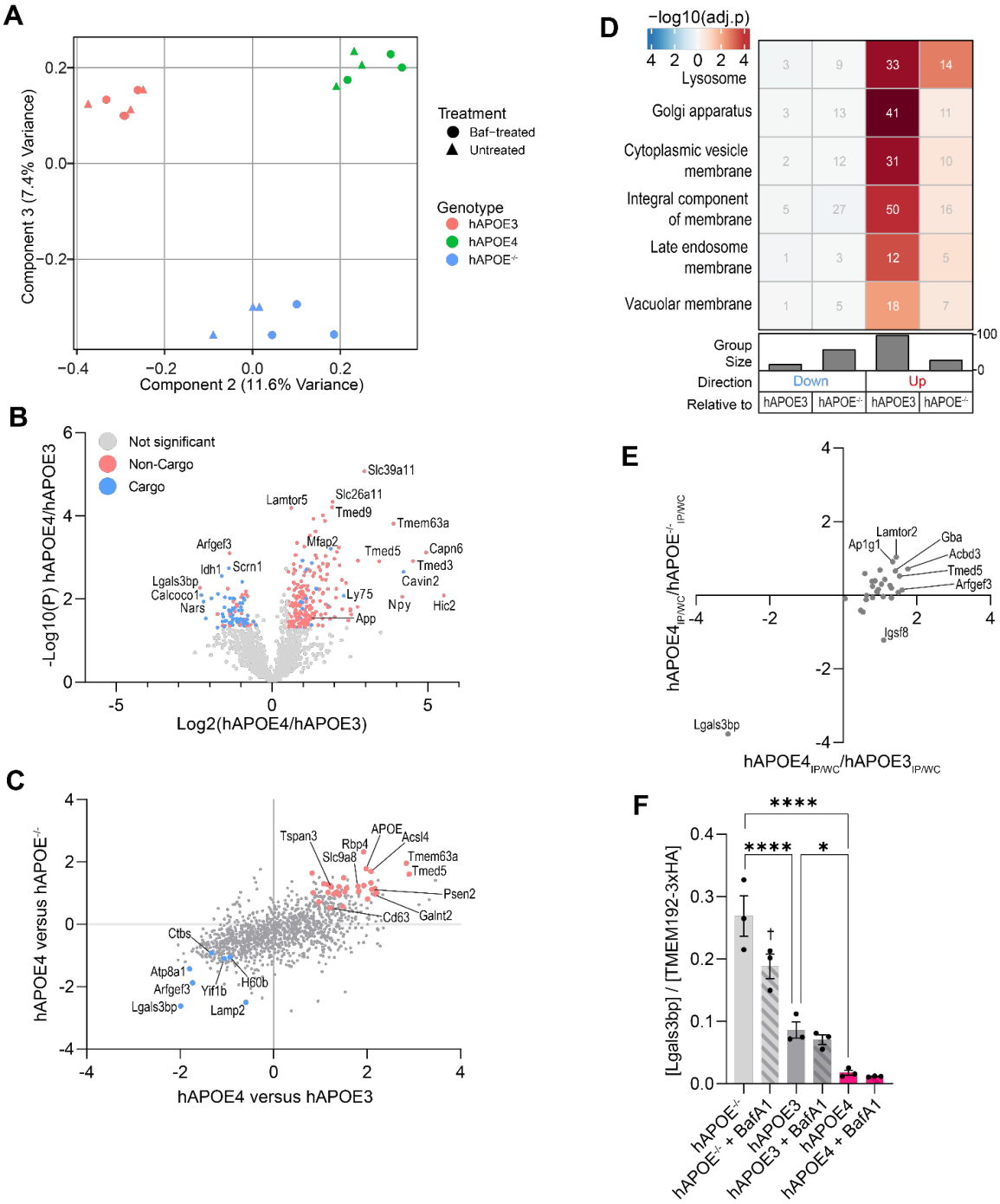

Figure 3: The apoE4-associated lysosomal proteome. (**A**) Principal component analysis separates Neuro-2a lysosomal proteomes by hAPOE genotype based on PCA components 2 and 3. (**B**) Volcano plot showing hAPOE4-associated lysosomal protein changes relative to hAPOE3 controls. Proteins significantly changed in hAPOE4 lysosomes are colored by their status as a lysosomal cargo protein, based on basal (red) or BafA1-dependent (blue) lysosomal enrichment. (**C**) Correlation of hAPOE4-associated lysosomal protein changes relative to both hAPOE3 and hAPOE$^{-/-}$ controls. Axes are geometric means of Log2(hAPOE4/control) and -Log10(P) values, calculated using the formula $Geometric\ Mean = \sqrt{Log2\left(\frac{hAPOE4}{Control}\right) * -Log_{10}(P)}$. Colored proteins were statistically significantly ($p < 0.05$) depleted (blue) or accumulated (red) in hAPOE4 lysosomes relative to both controls. (**D**) Enrichment of gene ontology (GO) terms associated for hAPOE4-associated lysosomal proteins as compared to hAPOE3 or hAPOE$^{-/-}$ lysosomal proteins. (**E**) Lysosomal protein distribution coefficients ($[Protein]_{Lysosome}/[Protein]_{Whole\text{-}cell}$) in hAPOE4 lysosomes relative to hAPOE3 and hAPOE$^{-/-}$ controls. (**F**) Protein abundance of lysosomal Lgals3bp as factor of hAPOE expression, allele, and BafA1 proton pump blockade. The data was analyzed in GraphPad Prism by 2-way ANOVA followed *post-hoc* by Bonferroni's multiple comparisons test. *P<0.05; ****P<0.0001.

After demonstrating successful enrichment of lysosomal proteins, we next investigated the consequences of apoE4 expression on the lysosomal proteome, particularly in light of the lysosomal disturbances observed in hAPOE4-expressing cells (Table S1D-E). Lysosomal proteomes could be readily separated by genotype both by principal component analysis (PCA; Fig. 3A) and hierarchical clustering (Fig. S3A-B; Fig. 2C). PCA component 2 (11.6% variance) separated hAPOE3- and hAPOE4-expressing samples based on hAPOE4-associated accumulation of glucosyl hydrolases, Lamtor proteins, and a number of Golgi-associated vesicle proteins, while enzymes regulating aminoacyl-tRNA biosynthesis and gluconeogenesis were depleted. Component 3 (7.4% variance) separated hAPOE$^{-/-}$ lysosomes from hAPOE-expressing lysosomes, marked by hAPOE-dependent accumulation of sterol transporters and proton pump subunits, and a depletion of proteasome subunits and microtubule proteins (Fig. 3A). Comparing hAPOE4- to hAPOE3-expressing cells, we observed an increase in TMED proteins (Fig. 3B), implicated in ER-Golgi trafficking and sorting misfolded proteins to the lysosomes [64]. Intriguingly, most lysosomal proteins with lower abundance in hAPOE4 cells were Bafilomycin A1-sensitive proteins that accumulate upon proton pump blockade, including the phospho-Tau-binding protein Scrn1 (Fig. 3B) [65]. The few intrinsically lysosomal proteins expressed at lower levels in hAPOE4 lysosomes include the ADP ribosylation factor activator Arfgef3/Big3 regulating lysosomal trafficking [66] and the glycoprotein Lgals3bp/90K-BP/Mac-2BP (Fig. 3B).

Since we (and others) have found that neuronal apoE4 confers a gain-of-toxicity effect not observed in hAPOE$^{-/-}$ or hAPOE3 cells [9, 24, 67], we extended our comparisons of the lysosomal proteome to hAPOE$^{-/-}$ cells to identify lysosomal proteins differentially regulated uniquely in apoE4 cells. We considered proteins significant if they changed in the same direction and reached statistical significance relative to both hAPOE$^{-/-}$ and hAPOE3 controls. To illustrate the hAPOE4-dependent proteomic alterations relative to both controls simultaneously, we calculated the geometric mean of the P and log2(hAPOE4/control) values. Proteins that reached statistical significance relative to both controls are highlighted in Fig. 3C. Through this approach, we found that hAPOE4-expressing lysosomes accumulated APOE itself, AD-associated secretase proteins (Psen2, Cd63, Tspan3), trafficking adaptors (Ap1s1, Ap1g1, Bet1l, Lamtor1, Lamtor2, Tmed5), and lipid/glycan-regulators (Acsl4, Acbd3, Galnt2, Man2b1, Neu1, Pip4p1, Sacm1l, Tmem55b, Uxs1) (Fig. 3B-C, Fig. S4C). Proteins accumulating in hAPOE4 lysosomes were principally enriched in the “Lysosome” gene ontology (GO) term, even when correcting for the already lysosome-laden background proteome (Fig. 3D). Proteins annotated under the Golgi apparatus, particularly chaperones and proteins ensuring its structural integrity, also accumulated in hAPOE4 lysosomes (Fig. 3D). Fewer changes were observed in the opposite direction, with the hAPOE4-expressing lysosomes expressing lower levels of the aforementioned Arfgef3 and Lgals3bp among others (Fig. 3B-C, Fig. S4C-D).

Since lysosomal protein changes could be secondary to whole-cell expression changes, we correlated the expression level of dysregulated lysosomal proteins to their whole-cell abundance. As expected, we observed a robust correlation between hAPOE4-associated global and lysosomal protein level changes (Fig. S4E-F; Table S1F). We hypothesized that proteins that were over- or underrepresented on hAPOE4 lysosomes could reflect changes in their lysosomal uptake and/or clearance. For example, a lysosome-accumulating protein that decreases on the whole-cell level could reflect its increased trafficking to the lysosome, resulting in lysosomal degradation. Conversely, a protein depleted from lysosomes but accumulating in the whole-cell fraction could

suggest impaired lysosomal uptake, and result in its cellular accumulation. To explore such possibilities, we plotted lysosomal under- or overrepresented proteins in the context of the hAPOE4 genotype. Note, proteins not detected in whole-cell samples could not be plotted, precluding similar analyses of 15 proteins including Psen2 and Rbp4. This approach highlighted the unique case of Lgals3bp, a protein whose expression was reduced in lysosomes despite unchanged whole-cell expression levels (Fig. 3E). In contrast, several proteins were overrepresented in the lysosome, including Lamtor2, Ap1g1, Acbd3, and Tmed5, although these changes were less extreme. Performing a partial least squares discriminant analysis to identify proteins characteristically separating lysosomes of one genotype from others further highlighted Lgals3bp depletion to be a characteristic feature of hAPOE4-expressing lysosomes (Fig. S4G). Intriguingly, lysosomal Lgals3bp levels appeared sensitive to both hAPOE and proton pump blockade, with hAPOE$^{-/-}$ lysosomes boasting the highest Lgals3bp levels and BafA1 treated hAPOE4 lysosomes containing the least Lgals3bp (Fig. 3F). This approach thereby revealed a set of hAPOE4-dysregulated lysosomal proteins where lysosomal protein abundance changes were not indirectly driven by changes in whole cell expression, but rather directly driven by changes to how these proteins are recruited to and cleared from the lysosome.

Identification of drivers underlying lysosomal defects in apoE4 neurons

Having identified hAPOE4-sensitive lysosomal proteins, we assessed whether knockdown of these proteins affects lysosomal function. We targeted Lgals3bp as the only downregulated protein in hAPOE4 lysosomes, being the principal characteristic protein separating hAPOE4 lysosomes from hAPOE$^{-/-}$ and hAPOE3 lysosomes. We also targeted three major AD risk factor proteins that we found to be accumulating in hAPOE4 lysosomes, specifically apoE itself, App [68] and Psen2 [52]. We also targeted tau, as it interfaces with and spreads via the autophagic/lysosomal system [69–77], and is implicated across neurological disorders (tauopathies). Finally, we targeted Tmed5, which we observed to be one of the most significantly accumulating lysosomal proteins associated with Golgi apparatus functions.

We first validated the efficacy of our siRNAs in reducing transcript levels (Fig. S5A), and protein levels of our top candidates (Fig. S5B-C). We then assessed their influence on lysosomal function. We considered an accumulating lysosomal protein a hit if its knockdown increased Lysotracker staining in hAPOE4 cells, or a depleted lysosomal protein (Lgals3bp) if its removal reduced Lysotracker staining in hAPOE3 cells. This highlighted that the apoE4-associated lysosomal impairments could be driven by Lgals3bp depletion and Tmed5 accumulation (Fig. S5D).

ApoE4-associated lysosomal Lgals3bp depletion decreases the lysosomal density of neurons

We found that Lgals3bp depletion markedly decreased the Lysotracker staining in healthy hAPOE3 Neuro-2a cells (Fig. 4A-B). To assess whether this was driven by changes in lysosomal acidification or the density of lysosomes, we loaded the Neuro-2a cells with Dextran-Oregon Green, finding that Lgals3bp knockdown modestly alkalinized the lysosomal pH, but nearly halved the lysosomal density (Fig. 4C-E). To assess whether these changes were accompanied by altered lysosomal processing, we measured lysosomal proteolysis using MR-CtsB. In line with its modest influence on lysosomal acidification, we could not detect significant proteolytic impairments upon Lgals3bp knockdown (Fig. 4F-G). In order to examine if LGALS3BP depletion similarly decreases LysoTracker staining in post-mitotic, apoE3 human neurons, we used CRISPRi-encoding iPSCs

302 [78, 79] to generate mature neurons (iNeu). As a positive control, we inhibited TMED10, which
303 previously has been shown to enhance lysotracker staining [79]. We confirmed that while TMED10
304 inhibition increased lysotracker staining in iPSC-derived neurons, LGALS3BP inhibition decreased
305 staining, suggesting that LGALS3BP is necessary to maintain lysosomal integrity across neuronal
306 models (Fig. 4H-I).

307 While Lgals3bp has been explored in the context of centriolar function and its extracellular
308 secretion [80–83], little is known about how it affects lysosomal function. It structurally consists of
309 three domains: An N-terminal Scavenger Receptor Cysteine-Rich (SRCR) domain associated with
310 phagocytosis of negatively charged ligands such as lipoproteins [84], a BTB domain that recruits
311 ubiquitin ligase complexes, and a C-terminal BTB- and Kelch-associated BACK domain [85]. This
312 domain architecture suggests that Lgals3bp could scaffold SRCR substrates and ubiquitin ligases
313 associated with the BTB-BACK domain, facilitating substrate ubiquitination and degradation.
314 While Lgals3bp was recently described as a ubiquitous lysosomal protein [86], the lysosomal
315 function of Lgals3bp is largely unknown [86].

316 We set out to identify the determinants of the intracellular Lgals3bp mislocalization underlying the
317 hAPOE4-associated lysosomal depletion, and to identify putative Lgals3b-associated mediators of
318 lysosomal function. In order to do so, we evaluated the Lgals3bp interactome by affinity-
319 purification mass spectrometry (APMS; Table S2A-C). The obtained Lgals3bp interactomes readily
320 clustered away from the GFP interactomes, indicating a distinct interactome not governed by the
321 GFP affinity tag (Fig. S6D). Having identified Lgals3bp interactors, we used STRING [87] to
322 annotate protein complexes within the Lgals3bp interaction network (Fig. S6E). Lgals3bp-
323 associated proteins and protein complexes were next manually assigned subcellular compartments
324 (Fig. 4J). While studies have previously focused on its functions as a secretory [81–83] or centriole-
325 associated protein [80], Lgals3bp is associated with a diversity of protein complexes associated
326 with the nucleus, cytoskeleton, mitochondria, the endoplasmic reticulum (ER), and lysosomes. Of
327 particular interest, we find that Lgals3bp interacts with ER-to-lysosome-trafficking proteins, and
328 proteins regulating lysosomal acidification (specifically Atp6v1a and Atp6v1h).

329 A plausible explanation for the apoE4 allele-associated Lgals3bp depletion would be a changed
330 Lgals3bp interactome. Specifically, lower expression of its lysosome-routing proteins would result
331 in the observed lysosomal depletion. We therefore assessed whether apoE4 expression affected the
332 Lgals3bp interactome. Among a few altered interactors, we found that apoE4 favored interactions
333 between Lgals3bp and the ER-to-Golgi cargo receptor Tmed10, associated with a trend towards
334 higher Tmed10 expression (Fig. 4J-K; Table S2D-E). Conversely, the apoE4 allele context
335 decreased the interaction of Lgals3bp with several proteins, including Faf2 which is associated with
336 the lysosome-routing Vcp/ERAD machinery (Fig. 4J-K). Of note, Faf2 protein abundance is
337 significantly lower in hAPOE4 cells, which may serve as a mechanism to prevent the association
338 of Lgals3bp with this lysosome-routing interaction partner (Fig. 4K; Table S2F). Taken together,
339 we find that several Lgals3bp interaction partners are differentially regulated in hAPOE3 and
340 hAPOE4 cells, which has the potential to influence the localization and trafficking of Lgals3bp.

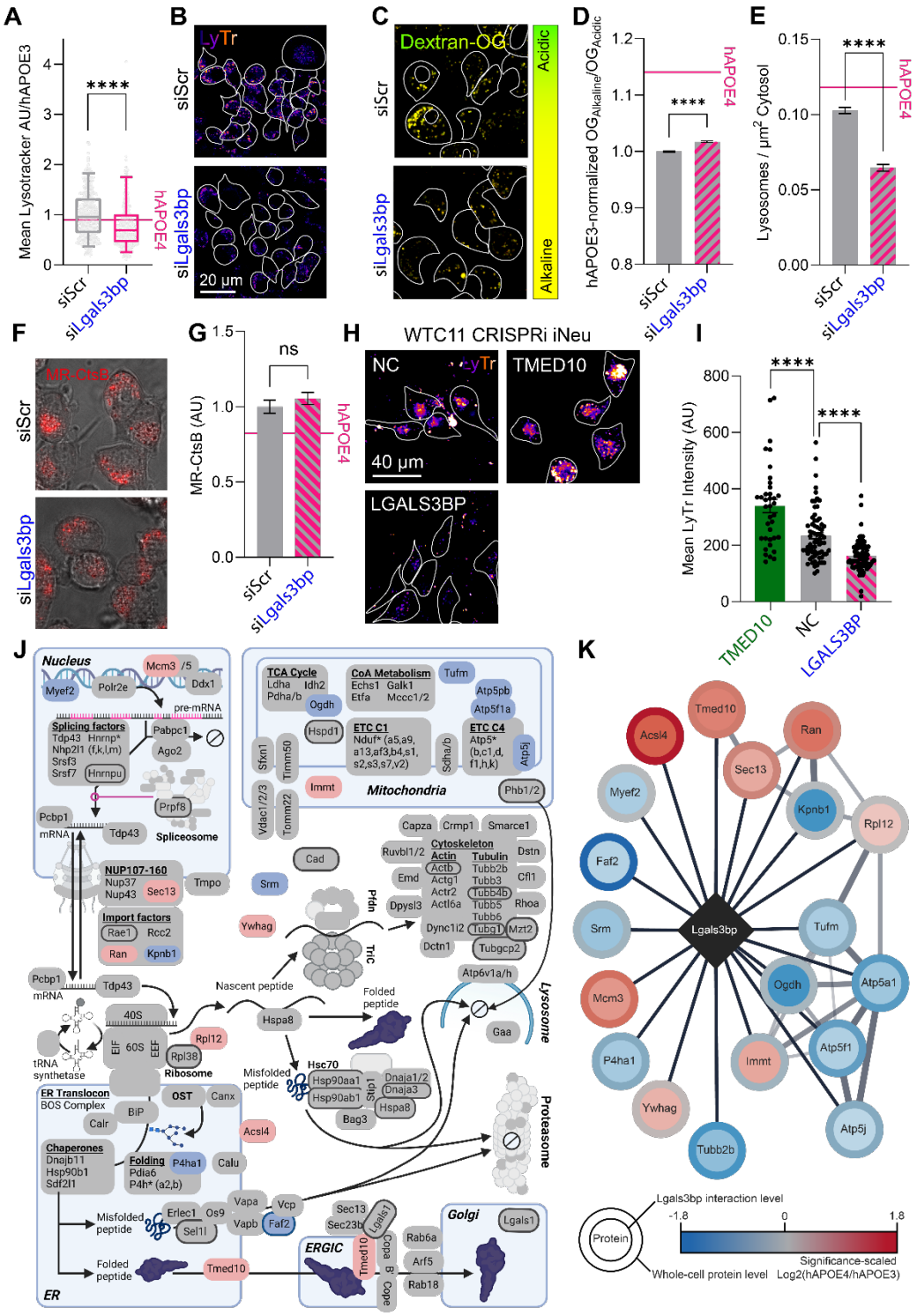

Figure 4: Local Lgals3bp depletion in hAPOE4 lysosomes affects the lysosomal density. (**A**) Quantification of LysoTracker staining of acidic compartments in hAPOE3 Neuro-2a cells following knockdown of Lgals3bp. Boxes indicate the 5-95 percentile. Data points indicate individual cells from three independent experiments. (**B**) Representative LysoTracker images for quantification shown in (A). (**C**) Oregon-green relative pH measurements upon Lgals3bp knockdown in hAPOE3 Neuro-2a cells, compared to scrambled controls. (**D-E**) Quantification of relative lysosomal pH (D) and density (E) upon Lgals3bp knockdown, as shown in panel (C). The value of these measurements in hAPOE4 Neuro-2a cells upon treatment with scrambled controls is shown for reference. Data is plotted as pH per lysosome or cellular lysosomal density across three independent experiments. (**F**) Magic Red Cathepsin B images of hAPOE3 Neuro-2a cells following Lgals3bp knockdown. (**G**) Quantification of Magic Red Cathepsin B intensity per cell across three independent experiments, as shown in panel (F). The value of this measurement in hAPOE4 Neuro-2a cells upon treatment with scrambled controls is shown for reference.

(**H**) Representative LysoTracker images of iPSC-derived neurons following CRISPRi suppression of indicated genes, relative to untransduced negative controls (NC). (**I**) Quantification of LysoTracker measurements per cell from panel H, measured across three independent experiments. (**J**) Proteins found to bind Lgals3bp are highlighted in their canonical cellular compartment. Grey interactors were unchanged by apoE genotype; colored protein nodes indicate preferential association with Lgals3bp in the context of apoE3 (blue) or apoE4 (red) genotypes. Nodes with borders are annotated Lgals3bp interactors by the BioGRID protein interaction repository [95]. The illustration was created with BioRender.com. (**K**) Cytoscape network of apoE genotype-associated Lgals3bp interactors. Fill colors represent relative retrieval of Lgals3bp interaction partners, with red indicating interactors with greater Lgals3bp binding in hAPOE4 Neuro-2a cells, and blue indicating interactors with greater Lgals3bp binding in hAPOE3 cells. Border colors represent relative protein abundances (hAPOE4/hAPOE3) in the whole-cell lysate. All experiments were performed as three technical and biological replicates. Fluorophore intensities and spot counting was performed in Fiji. Data was analyzed in GraphPad Prism by 2-way ANOVA followed *post-hoc* by Dunnett's multiple comparisons test. ****P<0.0001.

Increased Tmed5 expression causes lysosomal overflow and alkalinization in apoE4 neurons

In contrast to Lgals3bp, we found that apoE4-associated Tmed5 accumulation in lysosomes caused lysosomal defects that could be reversed by its acute removal (Fig. 5A-B). We confirmed by lysosomal Oregon-green pH measurements that knockdown of Tmed5 significantly enhanced lysosomal acidification in hAPOE4 Neuro-2a cells, while not impacting the lysosomal density (Fig. 5C-E). We subsequently continued to assess how this influence on lysosomal acidification affected lysosomal processing. We found that Tmed5 removal significantly enhanced lysosomal proteolysis of the MR-CtsB indicator in hAPOE4 cells (Fig. 5F-G). Concurrently, we found that Tmed5 knockdown significantly enhanced mitophagy in hAPOE4 Neuro-2a cells, shifting mitochondria towards more acidic environments both under basal and FCCP-induced conditions (Fig. 5H-I). Conversely, in hAPOE3 Neuro-2a cells we found that TMED5 overexpression caused the opposite phenotype, resulting in decreased LysoTracker staining (Fig. 5J-K) and lysosomal proteolysis (Fig. 5L-M). These findings indicate an intricate link between TMED5 expression levels, where its apoE4-associated overexpression causes lysosomal alkalinization and impairing lysosomal catabolism. They also corroborate TMED5 as a tunable target for modulating lysosomal activity, with its removal alleviating lysosomal impediments observed in apoE4 cells.

Taken together, we have identified two proteomic driving forces for apoE4-associated lysosomal dysfunction: On one hand, Tmed5 accumulates in apoE4 lysosomes, with its knockdown restoring lysosomal acidity. In contrast, Lgals3bp is depleted from apoE4 lysosomes, and its silencing in apoE3-expressing cells reduces the cellular lysosomal capacity (Fig. 5N). Changes to these lysosomal proteins thereby connect apoE4 expression with the observed lysosomal impairments (Fig. 5O).

Figure 5 (next page): Lysosomal Tmed5 overflow causes lysosomal alkalinization in hAPOE4 cells. (**A**) Quantification of LysoTracker staining of acidic compartments in hAPOE4 Neuro-2a cells following knockdown of Tmed5. Boxes indicate the 5-95 percentile. Data points indicate individual cells from three independent experiments. (**B**) Representative LysoTracker images for quantification shown in (A). (**C**) Oregon-green relative pH measurements upon Tmed5 knockdown in hAPOE4 Neuro-2a cells, compared to scrambled controls. (**D-E**) Quantification of relative lysosomal pH (D) and density (E) upon Tmed5 knockdown, as shown in panel (C). The value of these measurements in hAPOE3 Neuro-2a cells upon treatment with scrambled controls is shown for reference. Data is plotted as pH per lysosome or cellular lysosomal density across three independent experiments. (**F**) Magic Red Cathepsin B images of hAPOE4 Neuro-2a cells following Tmed5 knockdown. (**G**) Quantification of Magic Red Cathepsin B intensity per cell across three independent experiments, as shown in panel (F). The value of this measurement in hAPOE3 Neuro-2a cells upon treatment with scrambled controls is shown for reference. (**H**) Quantification of mitophagy by mtKeima measurements following Tmed5 knockdown in hAPOE4 Neuro-2a cells under basal and FCCP-induced conditions, plotted as a density plot of mitochondria across three independent experiments. The value of this measurement in hAPOE3 Neuro-2a cells upon treatment with scrambled controls is shown for reference. (**I**) Representative images for panel (H). (**J**) Quantification of LysoTracker staining of acidic

compartments in hAPOE3 Neuro-2a cells following human TMED5-GFP overexpression, Log2-normalized relative to untransfected negative controls (NC). Data points indicate individual cells from three independent experiments. (**K**) Representative LysoTracker images for quantification shown in (J). (**L**) Quantification of Magic Red Cathepsin B proteolysis in hAPOE3 Neuro-2a cells following human TMED5-GFP overexpression, Log2-normalized relative to untransfected hAPOE3 cells. Data points indicate individual cells from three independent experiments. (**M**) Representative Magic Red Cathepsin B images for quantification shown in (L). (**N**) Tabular representation of hypotheses. (**O**) Graphical representation of experimental results. All experiments were performed as three technical and biological replicates. Fluorophore intensities and spot counting was performed in Fiji. Groups of data were analyzed in GraphPad Prism by 2-way ANOVA followed *post-hoc* by Dunnett's multiple comparisons test. Pairs of data were analyzed by t-tests. *P<0.05, ****P<0.0001.

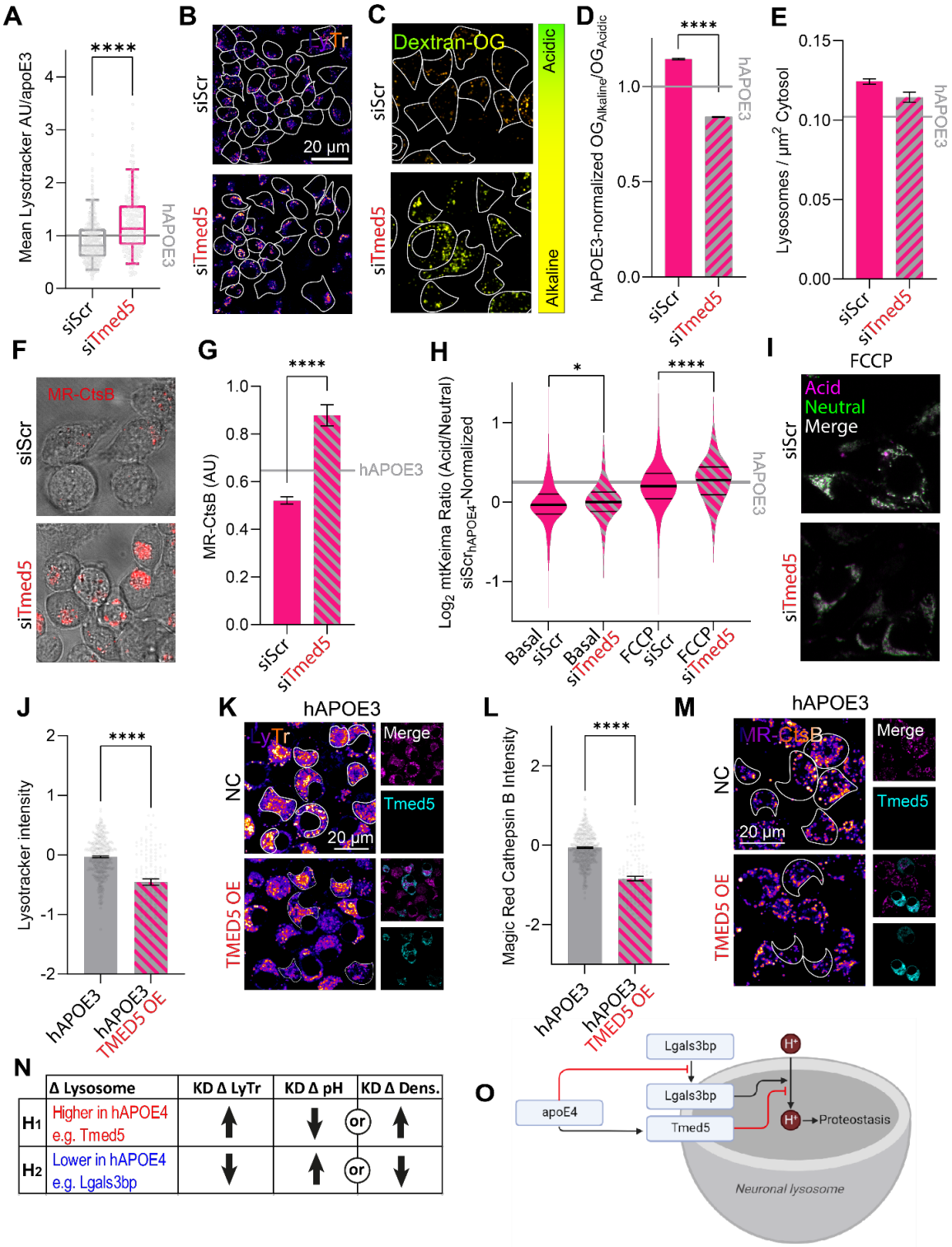

363

364 ***ApoE4 consistently modifies neuronal lysosomes across model systems***

365 Having observed that apoE4 expression impacts lysosomal function through Lgals3bp depletion
366 and Tmed5 accumulation, we evaluated their pathophysiological relevance in human iPSC-derived
367 neurons, neurons from *post-mortem* AD tissue, and apoE4 AD brains as a whole. In order to first
368 obtain cell-type resolution of lysosomal protein accumulation, we used isogenic apoE3 and apoE4
369 iPSCs to generate mixed neuronal cultures including GABAergic interneurons, which are
370 intimately linked to apoE4 neuropathology [24] (Fig. S7A). We profiled changes in lysosomal
371 LGALS3BP and TMED5 levels using a repurposed proximity ligation assay (PLA), illustrated by
372 Fig. 6A. PLAs are widely used to profile protein-protein interactions, yielding fluorescent signals
373 when the donor and acceptor proteins are within 40 nm of each other [88]. However, the lysosomal
374 lumen is a compact and protein-dense compartment, with a radius ranging from 100-300 nm [89,
375 90]. We reasoned that coincidental interactions between the reference lysosomal protein LAMP1
376 and our proteins of interest would occur more frequently in the lysosomal lumen and be detectable
377 by proximity ligation. In agreement with this hypothesis, we found that the LAMP1-LAMP1
378 positive control yielded a particularly good signal-to-noise ratio over the single-antibody controls,
379 whereas the LAMP1-LGALS3BP and LAMP1-TMED5 yielded comparatively less efficient, yet
380 still significant, lysosomal PLA signals (Fig. S7B-C). Having established that we could detect
381 lysosomal LGALS3BP and TMED5, we compared lysosomal PLA signals between apoE3 and
382 apoE4 human iPSC-derived neurons. In concordance with our observations in Neuro-2a cells, we
383 found that apoE4 iPSC-derived neurons harbored less lysosomal LGALS3BP and more lysosomal
384 TMED5 compared to their apoE3 counterparts (Fig. 6B-C). We subsequently utilized the same
385 assay to assess whether these lysosomal protein changes also occur in *post-mortem* brain slices
386 from AD patients. For LGALS3BP, the PLA signal was generally low, perhaps indicative that its
387 lysosomal depletion could be a wider phenomenon occurring in late-stage AD independently of the
388 apoE4 genotype. While we observed a general trend of lower lysosomal LGALS3BP levels in
389 apoE4 neurons, this was not statistically significant (P=0.24; Fig. 6D-E). On the other hand, we
390 found that neurons from apoE4 AD brain samples accumulate lysosomal TMED5, indicating that
391 lysosomal TMED5 accumulation is a highly conserved event in apoE4 neuropathology (Fig. 6F-
392 G).

393 We finally assessed whether the implicated apoE4-dysregulated lysosomal proteins from our
394 LysoIP experiments are conserved across large-scale studies using proteomic datasets from the
395 Accelerating Medicines Partnership – Alzheimer Disease (AMP-AD) consortium [91]. In analogy
396 with our observations that hAPOE4-encoding cells accumulate lysosomal proteins, we first
397 investigated how AD progression affects the lysosomal proteins we identified. Proteomic data from
398 the Baltimore Longitudinal Study of Aging (BLSA) cohort revealed a significant positive
399 correlation between apoE4 lysosome-associated proteins (Fig. 6H) with APOE4 dosage (Fig. 6I,
400 cor=0.37, p=3.6E-4). The same group of proteins were also significantly increased in AD vs
401 controls (Fig. 6J, p=0.03). Moreover, the Banner Sun Health Research Institute (Banner) cohort
402 revealed significant positive correlation between all apoE4-dysregulated lysosomal proteins
403 relative to apoE3 controls (Fig. 6K) with APOE4 dosage (Fig. 6L, cor=0.32, p=7.2E-6). These
404 dysregulated proteins similarly accumulated in AD patients compared to control and asymptomatic,
405 mild-cognitive impairment (MCI) patients (Fig. 6M, AD vs controls p=8.0E-16). Altogether, this

data suggest that dysregulated lysosomal proteins may play an important role in the human brain of APOE4 carriers.

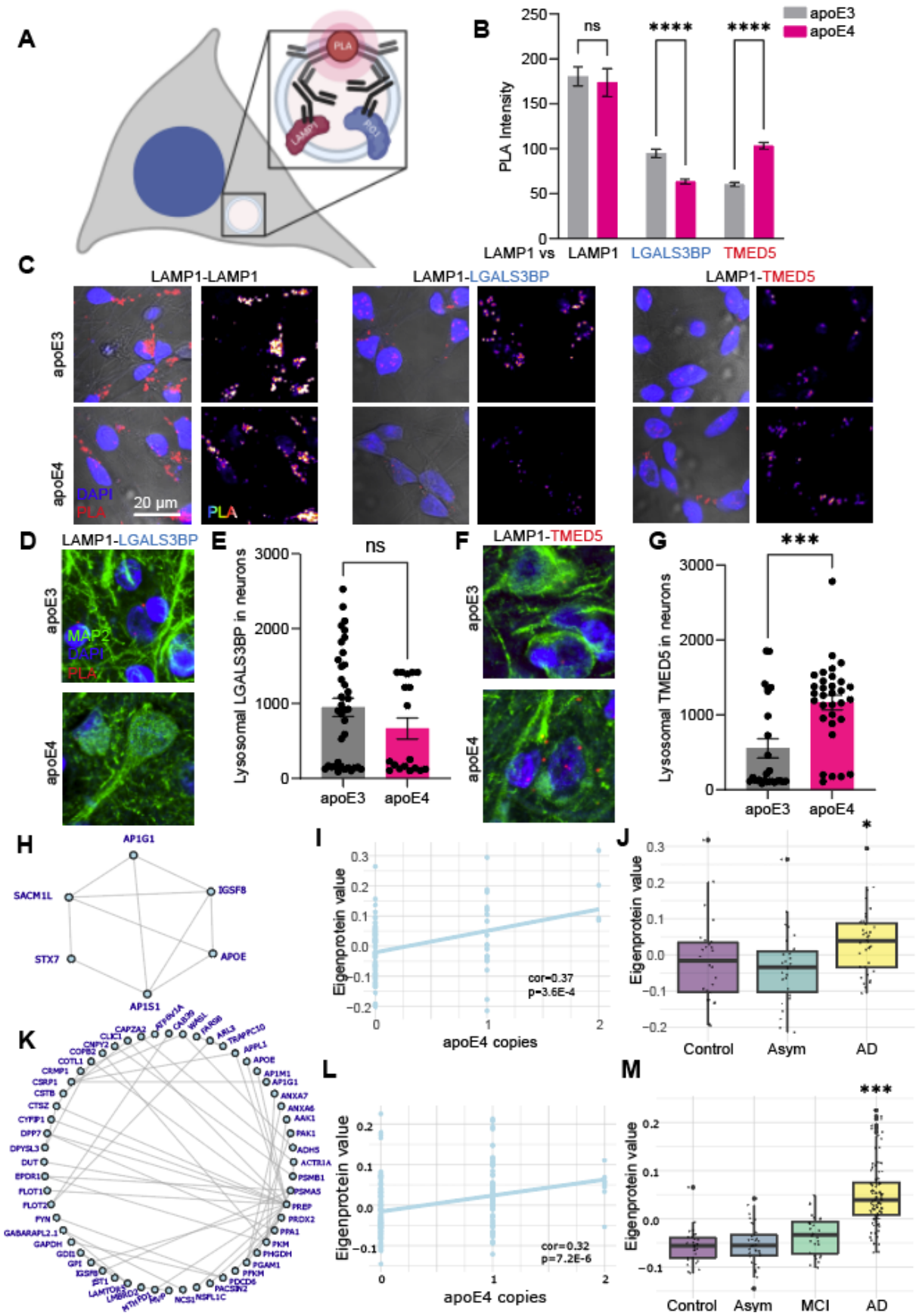

Figure 6 (previous page): ApoE4-associated lysosomal protein changes occur in human AD brains and neurons. (**A**) Schematic of lysosomal proximity ligation assay, whereby proximity ligation occurs between luminal lysosomal LAMP1 and the profiled protein of interest (P.O.I). (**B**) Quantification of cellular proximity ligation assay (PLA) signal in iPSC-derived neurons across three independent differentiations and experiments. LAMP1-LAMP1 was used as a positive control, while lysosomal LGALS3BP and TMED5 localization profiled by PLA with LAMP1. (**C**) Representative images for panel B. (**D**) Representative images of neuronal LGALS3BP-LAMP1 PLA in the AD brain. (**E**) Quantification of lysosomal LGALS3BP in the AD brain across two different cases per genotype, analyzed on a cellular level within a lysosomal mask based on PLA signal and LAMP1 immunoreactivity. (**F**) Representative images of neuronal TMED5-LAMP1 PLA in the AD brain. (**G**) Quantification of lysosomal TMED5 in the AD brain across two different cases per genotype, analyzed on a cellular level within a lysosomal mask based on PLA signal and LAMP1 immunoreactivity. (**H-J**) Plots showing apoE4 lysosome-associated proteins for individual patients from the BLSA cohort, showing (**H**) co-expression (nodes show dysregulated lysosomal proteins, edges denote highest protein co-expression), and their association with (I) APOE4 dosage and (**J**) AD diagnosis. (**K-M**) Plots showing apoE4-dysregulated lysosomal proteins for individual patients from the Banner cohort, showing (**K**) co-expression (nodes show dysregulated lysosomal proteins, edges denote highest protein co-expression), and their association with (**L**) APOE4 dosage and (**M**) AD diagnosis. *P<0.05; ***P<0.0005; ****P<0.0001.

These results illustrate that the apoE4-associated and functionally relevant lysosomal protein changes also manifest in human postmitotic neurons susceptible to neurodegeneration. Overall, these findings confirm that apoE4-associated lysosomal protein dysregulation occurs widely and consistently across AD model systems, including cell lines, iPSC-derived human neurons, and *post-mortem* brain samples.

Discussion

Regardless of its etiology, Alzheimer Disease is riddled with signs of impaired lysosomal function: In healthy neurons, lysosomes clear β-amyloid [92, 93], phospho-Tau aggregates [94], and dysfunctional organelles [95]. In the AD brain however, lysosomal dysfunction drives neuronal accumulation of AD-associated protein aggregates and defective organelles [96]. We find that neuronally encoded apoE4, the primary genetic risk factor for AD, impairs lysosomal function. It is established that astrocytes which express high apoE4 levels suffer from lysosomal alkalinization by unknown mechanisms [97]. While neuronal cells express less apoE4 than astrocytes, we observe a substantial degree of lysosomal alkalinization, which impairs both lysosomal proteolysis and mitophagy.

Focusing on the classical AD hallmark proteins App (forming toxic β-amyloid and β-CTF), we found that hAPOE4 lysosomes to accumulate App and the App-processing γ-secretase Psen2 subunit. This observation suggests that lysosomal defects could affect processing and aggregation of App. Indeed, it has previously shown that endocytic compartments are crucial in the amyloidogenic processing of App [98]. Intriguingly, we found that silencing *App* or its associated *Psen2* did not affect lysosomal function in hAPOE4-expressing cells, suggesting that rather than impairing lysosomal function itself, App accumulation may be downstream of hAPOE4-associated lysosomal impairments.

Our exploration of proteomic alterations to hAPOE4 lysosomes furthermore revealed that hAPOE4 lysosomes carry higher levels of lysosome- and Golgi-associated proteins. We furthermore observed that a select few of these functionally relevant protein changes also manifest in an apoE4 dose-dependent manner in both iPSC-derived human neurons and in AD *post mortem* brain samples, indicating the broader pathophysiological relevance of these observations. In line with

437 previous studies [56, 99], we found hAPOE4 to preferentially localize in lysosomes relative to its
438 hAPOE3 counterpart. This has been postulated as a route for hAPOE4 to escape the secretory
439 pathway, promoting its membrane interaction, cytosolic entry, and subsequent interference with
440 intracellular processes [99–101].

441 Intriguingly, hAPOE4 expression causes lysosomal accumulation of several Golgi-associated
442 Transmembrane emp24 domain-containing (Tmed) proteins, including Tmed3, Tmed4, Tmed5,
443 and Tmed9. Numerous Tmed proteins have been shown to be dysregulated in mild cognitive
444 impairment (MCI) and AD brains: While TMED5 expression increases in the AD parietal cortex
445 [102], expression of both TMED4 and TMED9 decreases in the AD frontal cortex [103–105]. Tmed
446 proteins regulate processing of secretory proteins and have been primarily studied in the context of
447 coatomer (COP) cargo selection and vesicle formation. However, Tmed proteins also have roles in
448 later secretory compartments [106]. In particular, Tmed5 and Tmed9 have been implicated in
449 trafficking misfolded GPI-anchored proteins from the plasma membrane to the lysosome, alongside
450 Tmed2 and Tmed10 [64]. In line with our own findings, knockdown of TMED2 and TMED10 in
451 human iPSC-derived neurons results in increased lysotracker staining [79], highlighting that the
452 coupling of TMED-family protein expression and lysosomal function is a widely conserved
453 phenomenon.

454 There is growing evidence that Lgals3bp may have diverse functional roles. Lgals3bp has been
455 studied in the context of cancer biology, and more recently, its neurological involvement has been
456 described in the process of neurodevelopmental corticogenesis. In concordance to our findings in
457 hAPOE4 lysosomes, Lgals3bp expression appears decreased post-in mortem in the Alzheimer
458 Disease entorhinal cortex [107]. While its lysosomal function remains uncharacterized, recent
459 proteomics experiments have demonstrated this protein to be consistently recovered from
460 lysosomes across cell lines [86]. Our results support these previous findings of Lgals3bp as a
461 lysosomal protein and provide insights into how it affects lysosomal function. Specifically, we
462 genetically decreased Lgals3bp expression in hAPOE3 cells, finding that Lgals3bp maintains
463 lysosomal density, and to a lesser extent lysosomal acidity. As Lgals3bp has been localized to
464 extracellular vesicles that form in late endosomal or lysosomal compartments [108] and suppresses
465 endosomal β-amyloid production [109], it is conceivable that Lgals3bp mediates lipid sequestration
466 and fine-tunes β-amyloid generation to prevent β-amyloid-mediated lysosomal damage. We
467 furthermore find Lgals3bp to interact with several subunits of the ER-associated degradation
468 (ERAD) machinery, which routes misfolded proteins from the ER towards lysosomes. We show
469 that hAPOE4 particularly impairs the interaction between Lgals3bp and the ERAD-associated E3
470 ubiquitin ligase-adaptor Faf2/Ubxd8 through decreasing Faf2 expression [110]. Decreased Faf2
471 expression has also been shown to facilitate tau seeding [111], indicating that apoE4-sensitive
472 ERAD proteins could be drivers for a host of AD-associated proteostatic and neuropathologic
473 events.

474 Importantly, while we find that while lysosomal Lgals3bp and Tmed5 are both differentially
475 regulated by apoE4 expression, their impact on lysosomal function is not limited to the context of
476 apoE4. Instead, increased Lgals3bp and decreased Tmed5 may be characteristic of lysosomal health
477 and capable of regulating lysosomal function. This is exemplified by targeted Lgals3bp knockdown
478 resulting in decreased lysosomal density and acidification in apoE3-expressing cells, and CRISPRi-

479 mediated knockdown of several TMED-proteins increasing lysotracker staining in wild-type iPSC-
480 derived neurons [79].

481 Taken together, we show that lysosomal dysfunction is not limited to early-onset forms of
482 Alzheimer Disease, but also occurs in the more common late-onset disease variant. We show that
483 apoE4 expression impairs lysosomal function in neuronal cells, describe novel mediators of
484 lysosomal pH homeostasis, and highlight their involvement in AD pathophysiology in patients and
485 across experimental models. Lysosomal pH dysregulation occurs in a number of diseases beyond
486 Alzheimer Disease including Parkinson's Disease, lupus, infectious diseases, cancers, and diabetes,
487 and a better understanding of the processes underlying these phenomena bears promise of broad
488 translational impact [112]. Our findings also implicate apoE4 and tau accumulation as a possible
489 contributor to lysosomal dysfunction in neurons, and provide a rationale for expanding therapeutic
490 trials targeting the lysosomal system to late-onset Alzheimer Disease.

491 Materials and Methods

492 *Plasmids*

493 The vector encoding the lysosomal calcium sensor LAMP2-GCaMP6s (pBoBi-hLAMP2-C-GC6s)
494 was obtained from Addgene (Addgene #154151). The lentiviral packaging vector pΔ-NRF Gag-
495 Pol-Tat-Rev and the pseudotyping vector pMD2.G VSV-G were kindly provided by Prof. Judd
496 Franklin Hultquist of Northwestern University. The lentiviral vector used for lysosomal
497 immunoprecipitation pLJC5-TMEM192-3xHA (Addgene #102930)[63] was kindly provided by
498 Dr. Ali Ghoochani and Prof. Monther Abu-Remaileh of Stanford University. The pCAGGS
499 mtKeima construct [113] was kindly provided by Dr. Huihui Li and Prof. Ken Nakamura of the
500 Gladstone Institutes. The mouse Lgals3bp-GFP construct was cloned by Gibson Assembly. Mouse
501 Lgals3bp was cloned from Neuro-2a cDNA using Q5 polymerase following the manufacturer's
502 instructions, annealing at 61.2°C with the forward primer
503 caagcttcgaattcagggacATGGCTCTCCTGTGGCTC and the reverse primer
504 cctgtggagccggtggagccCACCATGTCAGTGGAGTTAG. The pEGFP-N3 backbone was subcloned
505 from the LAMP1-mGFP plasmid (Addgene #34831) [114] using the forward primer
506 GGCTCCACCGGCTCCACA and the reverse primer GTCCCTGAATTCGAAGCTTGAGCTC.
507 Gibson Assembly was completed using the NEBuilder HiFi DNA Assembly Master Mix (NEB #
508 E2621L), following the manufacturer's instructions.

509 *Neuro-2a Cell Culture*

510 The murine, male neuroblastoma cell line Neuro-2a was previously modified by introducing
511 transgenic, full-length human apoE3 or apoE4 (herein referred to as hAPOE3 and hAPOE4,
512 respectively) [115]. The parental cell line without human apoE expression is referred to as hAPOE^{-}
513 $^{/-}$, referring to its human apoE genotype. Notably, the murine *Apoe* gene is intact in these cells.
514 Neuro-2a cells were cultured in sterile-filtered minimum essential medium + GlutaMAX (MEM,
515 ThermoFisher #41090-036) supplemented with 10% fetal bovine serum (FBS, ThermoFisher
516 #A31605-02), 1X non-essential amino acids (NEAA, ThermoFisher #11140050), and 1 mM
517 sodium pyruvate (ThermoFisher, #11360070). Cells were passaged using Accutase (Fisher
518 Scientific, #NC9839010) and used between passages 5-10.

519 ***Lipofectamine Transfection***

520 Cells were transfected using Lipofectamine 2000 (ThermoFisher #11668019) following the
521 manufacturer's protocols. Cells were cultured to 70% confluency prior to transfection. For transient
522 transfection, DNA was diluted in OptiMEM to 32 ng/µL and gently mixed. Lipofectamine 2000
523 was similarly diluted in OptiMEM to 8%, and both mixtures incubated for 5 minutes at room
524 temperature. Following the 5 minutes, DNA-OptiMEM and Lipofectamine-OptiMEM mixtures
525 were combined 1:1, gently mixed, and incubated for 20 minutes at room temperature. The
526 transfection mixture was subsequently added to the cells at a 1:6 mixture-to-media ratio, and the
527 cells transfected overnight. The media was replaced the following day, and the cells were
528 subsequently used for experiments. For siRNA knockdown, we targeted the following genes with
529 the indicated siRNAs (available from ThermoFisher): APOE (AM16708_41598), *App* (s62516),
530 *Lgals3bp* (AM16708_162469), *Mapt* (s70123), *Psen2* (AM16708_68876), scramble control
531 (4390844), and *Tmed5* (AM16703_83238). siRNAs were diluted in OptiMEM to 0.5 µM, and
532 Lipofectamine RNAi Max (ThermoFisher #13778150) diluted in OptiMEM to 5%. siRNA and
533 Lipofectamine mixtures were left for 5 minutes before being combined, and incubated for 20
534 minutes at room temperature. Following incubation, transfection mixtures were added to the wells
535 at a final concentration of 10% v/v. The cells were first transfected overnight, followed by a
536 complete medium exchange and a second subsequent transfection. The cells were used for
537 experiments after 48 hours knockdown in total.

538 ***RNA extraction, cDNA synthesis and RT-qPCR***

539 We used RT-qPCR to quantify the knockdown efficiencies of our siRNAs. Following 48 hours
540 knockdown, RNA was extracted using the RNeasy Kit (Qiagen #74106), following manufacturers'
541 instructions, supplementing RLT buffer with β-mercaptoethanol, homogenizing samples by
542 vortexing and without performing gDNA digestion. cDNA was reverse transcribed using the
543 Superscript IV kit (ThermoFisher #18090010), using 1 µg RNA as template, a 0.5:0.5 mixture of
544 Oligo d(T) and random hexamers for priming. The reaction was performed as follows: 10 minutes
545 hexamer annealing at 23°C, 10 minutes amplification at 55°C, and 10 minutes inactivation at 80°C.
546 Reverse-transcribed cDNA was diluted 1:10 with water. RT-qPCR was run using Power SYBR
547 Green PCR Master Mix (Thermo Fisher #4367659) to detect APOE as previously described [116],
548 and TaqMan (ThermoFisher #4444963) to detect *App* (Mm01344172_m1), *Hprt* (housekeeping
549 control; Mm01545399_m1), *Lgals3bp* (Mm00478303_m1), *Mapt* (Mm00521988_m1), *Psen2*
550 (Mm00448405_m1), and *Tmed5* (Mm00547008_m1). RT-qPCR reactions were performed on a
551 CFX Opus 96 real-time PCR system (BioRad) with the following cycling parameters: [95°C,
552 10:00],40x[95°C, 0:15; 60°C, 1:00] for SYBR reactions, [50°C, 2:00; 95°C, 10:00],40x[95°C, 0:15;
553 60°C, 1:00] for TaqMan reactions. Expression levels were analyzed by the $2^{-\Delta\Delta Ct}$ approach, using
554 *Hprt* as a housekeeping gene and scramble control samples as the treatment control.

555 ***Immunofluorescence and Confocal Microscopy***

556 Neuro-2a cells were seeded onto poly-L-lysine-coated (Sigma #P4707) 12 mm glass coverslips for
557 confocal microscopy and cultured as previously described. Cells were washed once with PBS
558 (Corning #21-030-CV) before they were fixed with 4% paraformaldehyde (Sigma #F8775). For
559 lysosomal immunostaining, cells were washed three times with PBS, and simultaneously
560 permeabilized and blocked for 1 hour at room temperature in a saponin-based blocking buffer (BB-

561 S; PBS with 1% BSA, 0.05% Saponin, 50 mM NH_4Cl, and 1% NaN_3). The cells were stained with
562 mouse anti-HA antibodies (BioLegend #901501) diluted 1:1000, rat anti-mouse Lamp1 antibodies
563 (SantaCruz #sc-19992) diluted 1:100, mouse anti-human LAMP1 antibodies (SantaCruz #sc-
564 20011) diluted 1:800, or rabbit anti-phospho-Tau(S202/T205) (ABclonal #AP0894) diluted 1:1000
565 in BB-S overnight at 4ºC, washed three times with PBS, and stained with either anti-mouse
566 Alexa488- (ThermoFisher #A11001)-, anti-rabbit Alexa488 (ThermoFisher #A21206)-, anti-mouse
567 Alexa555 (#A31570)-, anti-rabbit Alexa555 (ThermoFisher #A21428)-, or anti-rat fluorescein
568 (Vector #FI-4000)-conjugated secondary antibodies diluted 1:500 in BB-S for 2 hours at room
569 temperature. For iPSC-derived neuron immunostaining, cells were similarly fixed in 4% PFA for
570 15 minutes, and washed once with PBS. Cere washed once with washing buffer (PBS with 0.1%
571 Tween-20), and blocked with blocking solution (PBS with 10% donkey serum and 0.5% Triton-X)
572 for 1 hour. Cells were stained overnight at 4°C with rabbit anti-GABA (ThermoFisher #PA5-32241)
573 diluted 1:1000 and mouse anti-TuJ (Promega #G712A) diluted 1:1000 in PBS with 1% donkey
574 serum. Cells were washed twice with washing buffer, and stained with aforementioned secondary
575 antibodies for 1 hour in PBS with 1% donkey serum. Cells were again washed twice with washing
576 buffer. Nuclei were subsequently stained for by incubation with 200 ng/mL Hoechst 33342
577 (ThermoFisher #H3570) diluted in PBS for 30 minutes at room temperature. The samples were
578 washed three times with PBS and mounted onto Micro Slides (VWR #48311-703) using Cytoseal™
579 60 (VWR #8310-4). Images were captured using a confocal laser scanning microscope (Zeiss
580 LSM880) fitted with a Plan-Apochromat 63x/1.4 Oil DIC M27 objective and PMT detector. Nuclei
581 were imaged by excitation at 405 nm and detection between 410-507 nm, with the pinhole set to
582 1.36 AU. The AlexaFluor488-stained lysosomal tags were imaged by excitation at 488 nm and
583 detection between 493-630 nm, with the pinhole set to 0.43 AU. Pixel scaling was set to 70 nm to
584 capture lysosomal structures.

585 ***Lysotracker Imaging***

586 The lysosomal expanse of the Neuro-2a cells was determined using the Lysotracker probe. Neuro-
587 2a cells were seeded into live-cell imaging chambers (ibidi #80806) at a density of $2*10^5$ cells/mL.
588 The media was exchanged for fresh media on day 2 of culture. On day 3, the cells were stained with
589 Lysotracker Red DND-99 (ThermoFisher #L7528) diluted 1:10,000 to label acidic endolysosomes
590 and CellMask™ Deep Red Plasma Membrane Stain (ThermoFisher #C10046) diluted 1:1000 to
591 label the plasma membrane. The cells were loaded for 30 minutes at 37ºC before being chased in
592 culture media not containing staining reagents. The cells were transferred to a confocal laser
593 scanning microscope (Zeiss LSM880) fitted with a Plan-Apochromat 63x/1.4 Oil DIC M27
594 objective and PMT detector, with its incubation chamber pre-heated to 37ºC and atmosphere filled
595 with 5% CO_2. Lysotracker staining was imaged by excitation at 561 nm and detection between 566-
596 639 nm, with the pinhole set to 0.81 AU. CellMask staining was imaged by excitation at 633 nm
597 and detection between 639-759 nm, with the pinhole set to 0.93 AU. Pixel scaling was set to 90 nm
598 to capture lysosomal structures. Image analysis was performed in Fiji. The CellMask channel was
599 used to manually draw regions of interest (ROIs) delimiting individual cells, and the roiManager
600 Measure function used to measure the Lysotracker staining intensity of each cell. The results shown
601 were obtained from three distinct biological and technical replicate experiments.

602 ***pH Measurements using Oregon Green***

603 The lysosomal pH was accurately determined using the Oregon Green probe. Neuro-2a cells were
604 seeded into live-cell imaging chambers (ibidi #80806) at a density of $2*10^5$ cells/mL. On day 3, the
605 cells were loaded with 500 µg/mL OregonGreen™ 488; Dextran 70,000 MW (ThermoFisher
606 #D7172) overnight. The following day, the cells were chased in culture medium for 1 hour, before
607 0.1% DMSO (Sigma #D2650) or 200 nM Bafilomycin A1 (FisherScientific #AAJ61835MCR) was
608 added for another hour. The cells were transferred to a confocal laser scanning microscope (Zeiss
609 LSM880) fitted with a Plan-Apochromat 63x/1.4 Oil DIC M27 objective and PMT detector. pH-
610 insensitive, reference OregonGreen™ 488 staining was imaged by excitation at 458 nm and
611 detection between 495-605 nm. pH-sensitive OregonGreen™ 488 staining was imaged by
612 excitation at 488 nm and detection between 495-605 nm. The pinhole was set to 1.14 AU, and pixel
613 scaling set to 135 nm to capture lysosomal structures. After capturing 7 images of each condition,
614 the lysosomes were pH-clamped using the Intracellular pH Calibration Buffer Kit (ThermoFisher
615 #P35379), with its range expanded to include 10 different pH values ranging from pH 3.60 to pH
616 7.50, adjusting the buffer pH with HCl. The buffer kit was used following the manufacturer's
617 instructions, adding buffers starting at pH 7.50 and progressively adding more acidic buffers. One
618 calibration image was captured for each pH buffer. Image analysis was performed in Fiji. The
619 CellMask channel was used to manually draw single regions of interest (ROIs) delimiting cells. A
620 mask was generated of endosomes by using the 456 nm reference channel. A minimum filter was
621 first applied followed by a maximum filter (radius=3). The Li AutoThreshold function was used to
622 create a binary mask of lysosomes, followed by a dilation of the cell mask using EDM Binary
623 Operations (iterations=3). The Watershed function was used to divide lysosome clusters, and the
624 mask used to create a region of interest. The region of interest as split into its individual constituents,
625 and the intensity of each individual ROI (endosome) measured from the raw, unprocessed image.
626 The ratio of pH-sensitive to pH-insensitive fluorescence was subsequently calculated for each
627 individual endosome. The same data analysis was performed for the pH-clamped lysosomes,
628 allowing extrapolation from Oregon Green ratios to their respective absolute pH values. The results
629 shown were obtained from three distinct biological and technical replicate experiments.

630 ***Calcium Imaging using LAMP2-GCaMP6s***

631 Neuro-2a cells were seeded into live-cell imaging chambers (ibidi #80806) and cells cultured to
632 confluence. Upon reaching confluence, the cells were transiently transfected for 48 hours with the
633 LAMP2-GCaMP6s construct [60] using Lipofectamine 2000 (ThermoFisher #11668019) following
634 the manufacturer's instructions. Following transgene expression, the medium was replaced with
635 Ca^{2+}-free standard bath solution (142 mM NaCl, 6 mM KCl, 2 mM $MgCl_2$, 5.5 mM Glucose, 1 mM
636 EGTA, 10 mM HEPES, pH 7.4). Cells were transferred to a Zeiss LSM880 confocal microscope
637 fitted with a Plan-Apochromat 63x/1.4 Oil DIC M27 objective and an Airyscan detector,
638 preequilibrated to 37°C and 5% CO_2. Calcium-bound GCaMP6s was imaged by excitation at 488
639 nm and detection between 415-735 nm. To facilitate high-speed imaging while maintaining
640 resolution of lysosomal structures, pixel scaling was set to 130 nm, the pinhole set to 2.31 AU, and
641 images captured every second for 250 seconds. Cells were treated with 200 µM GPN (Cayman
642 #14634) at 50 seconds, and with 4 µM Ionomycin (Cayman #10004974) at 150 seconds. At least
643 three movies of were captured for each technical replicate. Image analysis was performed in Fiji.
644 A region of interest was generated of transfected cells excluding the nuclei, delimiting the area to

645 be analyzed. The fluorescence intensity of each region of interest (cell) was measured over time
646 using the Fiji MultiMeasure function. The results shown were obtained from three distinct
647 biological and technical replicate experiments.

648 ***Mitophagy Measurements using mtKeima***

649 Neuro-2a cells were seeded into live-cell imaging chambers (ibidi #80806) at a density of $2*10^5$
650 cells/mL, and cells cultured to 70% confluence. Upon reaching 70% confluence, the cells were
651 transfected with the mtKeima construct[113, 117] using Lipofectamine 2000 (ThermoFisher
652 #11668019) following the manufacturer's instructions. The cells were transfected overnight, and
653 media changed the next day. Fresh media was added alongside compounds for treatment, including
654 0.1% DMSO, 10 µM FCCP (Sigma #SML2959), and 200 nM Bafilomycin A1. The cells were
655 incubated for 30 minutes prior to imaging. The cells were transferred to a confocal laser scanning
656 microscope (Zeiss LSM880) fitted with a Plan-Apochromat 63x/1.4 Oil DIC M27 objective and
657 PMT detector, with its incubation chamber pre-heated to 37ºC and atmosphere filled with 5% CO_2.
658 Neutral mtKeima was imaged by excitation at 488 nm and detection between 600-708 nm, while
659 simultaneously capturing transmitted light. Acidic mtKeima was imaged by excitation at 514 nm
660 and detection between 544-680 nm. The pinhole was set to 0.92 AU, and pixel scaling set to 90 nm
661 to capture mitochondrial structures. Five images were captured for each condition. Image analysis
662 was performed in Fiji. A region of interest was generated of transfected cells based on the
663 transmitted light, delimiting the area to be analyzed. A mask was generated of mitochondria by
664 using both mtKeima channels. A minimum filter was first applied followed by a maximum filter
665 (radius=3). The Li AutoThreshold function was used to create a binary mask of lysosomes, followed
666 by a dilation of the cell mask using EDM Binary Operations (iterations=3), watershed, and erosion
667 using EDM Binary Operations (iterations=3). The resulting mask was used to create a region of
668 interest. The region of interest as split into its individual constituents, and the intensity of each
669 individual ROI (mitochondrion) measured from the raw, unprocessed image. The ratio of acidic to
670 neutral mtKeima was calculated for each mitochondrion. The results shown were obtained from
671 three distinct biological and technical replicate experiments.

672 ***Lentiviral Production***

673 Lentiviruses were produced as previously described [118]. HEK293T were cultured in DMEM
674 (Corning #10-017-CV) supplemented with 10% fetal bovine serum (FBS, ThermoFisher #A31605-
675 02), 1 mM sodium pyruvate (ThermoFisher, #11360070), and 1X Penicillin-Streptomycin
676 (Corning, #30-002-CI), and used between passages 4-8. On day 1, $6*10^6$ cells were seeded in 50
677 mL culture medium in 15 cm dishes and allowed to adhere overnight. On day 2, transfection
678 mixtures were prepared by diluting 5 µg lentiviral delivery vector, 3.33 µg Gag-Pol-Tat-Rev
679 packaging construct, and 1.66 µg VSV-G envelope construct in 250 µL serum-free DMEM
680 (Corning #10-017-CV). 30 µL PolyJet In Vitro DNA Transfection Reagent (SignaGen #SL100688)
681 was similarly diluted in 250 µL serum-free DMEM, and incubated at room temperature for 5
682 minutes. Following the 5 minutes, DNA-DMEM and PolyJet-DMEM mixtures were combined 1:1,
683 gently mixed, and incubated for 25 minutes at room temperature. The transfection mixture was
684 subsequently added dropwise to the cells, plates swirled, and incubated for 72 hours. The
685 supernatant was harvested on day 5. The supernatant was collected, and cellular debris removed by
686 centrifugation at 400g for 5 minutes. The supernatant was subsequently filtered using a 0.45 µm

687 PVDF filter unit, and virions precipitated by adding 8.5% PEG-6000 and 0.3M NaCl followed by
688 2 hours incubation at 4ºC. Virions were pelleted by centrifugation at 2700 g for 20 minutes at 4ºC.
689 The supernatant was decanted, virions resuspended in 250 µL PBS, and aliquoted for long-term
690 storage at -80ºC.

691 ***Lentiviral Transduction***

692 Neuro-2a cells were transduced by lentiviral spinoculation. Neuro-2a cells were dissociated using
693 Accutase (Fisher Scientific, #NC9839010), and $3*10^4$ cells resuspended in 2 mL media. Polybrene
694 (Millipore #TR-1003-G) was added to the cells to a final concentration of 8 µg/mL alongside 100
695 µL concentrated lentivirus, and the cells centrifuged at 1000 g for 1 hour at room temperature. The
696 supernatant was aspirated, cells resuspended in 2 mL Neuro-2a media (described in Neuro-2a Cell
697 Culture section) and seeded in a single well of a 6-well tissue culture plate. The cells were cultured
698 for 48 hours post-transduction before selecting for transduced cells using 2 µg/mL Puromycin
699 (ThermoFisher #A1113802) for 3 days. Following antibiotic selection, the polyclonal cells were
700 passaged and expanded once before being frozen for further experiments.

701 ***Lysosomal Immunoprecipitation***

702 Lysosomal immunoprecipitations were performed in biological and technical triplicates as
703 performed as previously described [63] with minor alterations. Neuro-2a cells with each
704 combination of apoE genotype ($hAPOE^{-/-}$, hAPOE3, or hAPOE4) and lysosomal tag integration
705 (background or LysoIP-tagged) were seeded, with $2*10^6$ cells being seeded across two 15 cm dishes
706 per replicate. To distinguish intrinsically lysosomal proteins from lysosomal cargo destined for
707 degradation, two 15 cm dishes of LysoIP-tagged $hAPOE^{-/-}$, hAPOE3, and hAPOE4 Neuro-2a cells
708 were treated with 200 nM Bafilomycin A1 (ThermoFisher #AAJ61835MCR) for 3 hours,
709 preventing lysosomal degradation and enriching for lysosomal cargo. To harvest lysosomes, each
710 sample was individually processed from beginning to lysis. All following steps were performed on
711 ice or at 4ºC ambient temperature, unless otherwise stated. Magnetic anti-HA beads (ThermoFisher
712 #88837) were washed twice with KPBS (136 mM KCl, 10 mM KH_2PO_4, pH adjusted to 7.25).
713 Culture media was quickly decanted and rinsed twice with ice-cold KPBS. Cells were collected by
714 scraping and transferred to microfuge tubes. Cells were pelleted by centrifugation (1000g, 2 min),
715 and the supernatant aspirated. The cells were next resuspended in 950 µL KPBS, and 25 µL cell
716 suspension aliquoted into Protein LoBind tubes for whole-cell analysis. The remaining 925 µL cell
717 suspension was homogenized upon passing the entire volume through a 20G needle 10 times, and
718 efficient release of cellular organelles assessed under a phase contrast microscope. The homogenate
719 was transferred to a new microcentrifuge tube and centrifuged (1000g, 2 min) to pellet the plasma
720 membrane. The supernatant was transferred to a new microcentrifuge tube containing 150 µL
721 magnetic anti-HA beads and mixed once by pipetting. The organelles and beads were rocked at
722 1200 rpm for 3 minutes and transferred to a magnet for washing. The beads were incubated on the
723 magnet for 25 seconds before the supernatant was aspirated and replaced with fresh KPBS. The
724 beads were rocked at 1200 rpm for 10 seconds and returned to the magnet. These washes were
725 repeated three times, transferring the cells to Protein LoBind tubes for the final wash. Upon
726 aspirating the KPBS following the final wash, 300 µL modified SP3 lysis buffer [119] (50 mM
727 Tris-HCl, 50 mM NaCl, 1% SDS, 1% NP-40, 1% Tween 20, 1% Glycerol, 1% Sodium
728 Deoxycholate, 5 mM EDTA, 5 mM Dithiothreitol, 5 KU Benzonase, 1 Complete protease inhibitor;

729 modified by excluding Triton X-100) was added to the input and bead samples. Upon finishing
730 processing all samples, the samples were lysed by rocking at 65ºC for 30 min at 1200 rpm. LysoIP
731 samples were placed on the magnet for 25 seconds, and the supernatant transferred to fresh Protein
732 LoBind tubes to remove magnetic beads. The samples were alkylated by adding chloracetamide
733 (final concentration 10 mM) and shielded from light for 30 minutes. The alkylated samples were
734 vortexed, solubilized on ice for 20 minutes, and centrifuged at 16000g for 10 minutes. The soluble
735 supernatant was transferred to new tubes, and -20ºC acetone added in four-fold volume to
736 precipitate protein. The samples were briefly vortexed and incubated at -80ºC for 1 hour. Proteins
737 were pelleted by centrifugation (2000 g, 15 min), and the pellet washed twice with -20ºC acetone.
738 The samples were stored at -80ºC until mass spectrometric analysis.

739 ***Mass Spectrometry***

740 Dry, digested peptides, were resuspended in 0.1% FA and separated using Thermo EASY-nLC
741 1200 nano liquid chromatography setup. Separation was performed using a 15 cm long Bruker
742 PepSep column with a 150 µm inner diameter packed with 1.5um Reprosil Saphir C18 particles.
743 Mobile phase A was composed of a 0.1% formic acid solution, while mobile phase B was composed
744 of 0.1% formic acid with 80% acetonitrile. Samples were loaded onto the column at the maximum
745 flow rate possible with an upper pressure limit of 300 bar, with the gradient performed using a
746 stable flow of 600 nl/min. For LysoIP samples, mobile phase began at 2%, before increasing to
747 30% over 70 mins. Mobile phase B then increased to 35% over 8 minutes before increasing to 90%
748 B over 2 minutes and finishing with a wash at 90% B for 10 minutes. The gradient required a total
749 time of 90 minutes. For APMS samples, mobile phase began at 4% B before increasing to 35%
750 over 44 minutes. Mobile phase B then increased to 45% over 5 minutes before increasing to 88%
751 B over 1 minute and finishing with a wash at 88% for 10 mins. The gradient for APMS samples
752 required a total time of 60 minutes.
753
754 Eluting peptides were ionized using electrospray ionization from a PepSep stainless steel emitter
755 and analyzed using a Thermo Orbitrap Fusion Lumos mass spectrometer. For LysoIP samples
756 acquisition was performed in a data-independent (DIA) manner with a single survey scan from 350-
757 1200 m/z at 120,000 resolution, followed by 40 variable window (Table S3) MS2 scans at 30,000
758 resolution with stepped HCD using 32 +/- 5 NCE. Survey scans utilized an AGC target of 4e5 with
759 maximum injection time set to "Auto", while MS2 scan AGC target was set to 5e4 with a maximum
760 injection time of 54 ms. All scans were taken in the Orbitrap. For APMS samples, acquisition was
761 performed in a data-dependent (DDA) manner. Survey scans were taken from 350-1350 m/z at a
762 resolution of 240,000, with a normalized AGC target of 250%, and a maximum injection time 50
763 ms. Dependent MS2 scans were collected in the ion trap from 200-1200 m/z using the "rapid" scan
764 speed, with a normalized AGC target of 300%, a "dynamic" maximum injection time, and an
765 isolation window of 0.7 m/z. Ions were activated using HCD with 32 NCE. Only ions with charge
766 state 2-5 were selected for fragmentation and ions were excluded with a 10 ppm tolerance for 20
767 seconds after being isolated for MS2 scans twice. MS system suitability was monitored with
768 QCloud2 [120].
769
770 For APMS samples, raw files were searched in MaxQuant using default parameters against a full
771 reviewed mouse proteome including isoforms (downloaded from Uniprot on June 6, 2022) to which

human APOE and TMEM192 proteins were added. The evidence.txt output table from that search was then used to generate the three tables necessary for SAINTexpress scoring (baits, preys, and interactions) using the artmsEvidenceToSaintExpress function from the artMS package (release 3.17) in R (version 4.1.1). Two sets of bait, prey, and interaction tables were generated, one using spectral counts and the other using intensity, with GFP samples set as the control group. Interactions were scored using SAINTexpress (version 3.6.3). Protein interactions were identified as significant if they resulted in a BFDR < 0.05 in either spectral count- or intensity-based SAINT analysis, and the prey protein was observed in all three replicates of that hAPOE-bait group (e.g., all Lgals3bp-GFP/hAPOE3, or all Lgals3bp-GFP/hAPOE4 samples). For these significant interactors we calculated protein fold change and significance when comparing the two alleles (Lgals3bp-GFP/hAPOE3 vs. Lgals3bp-GFP/hAPOE4) using the LFQ intensity from the proteinGroups.txt output table from MaxQuant. The identified Lgals3bp interaction partners and their quantification between apoE alleles are provided in Table S2.

For LysoIP samples, the resulting raw files were searched using directDIA in Spectronaut against a full reviewed mouse proteome including isoforms (downloaded from Uniprot on June 6, 2022) to which human APOE and TMEM192 proteins were added. Default search parameters were used without cross-run normalization or imputation. The resulting MSstats-formatted report was then used to summarize abundance at the protein level using Tukey's median polish after median normalization of peptide features [121]. Proteins were annotated as being lysosomal if they fulfilled one of two conditions: Either they were detected in three tagged replicates but undetected in untagged controls, or they were more than 2-fold enriched in lysosomes over the background, and reaching statistical significance. If proteins were only passing these criteria in Bafilomycin A1-treated samples, they were annotated as being lysosomal cargo. A subset of correlated peptide ions specific for human TMEM192 were selected for quantification of TMEM192 protein, to allow for the most accurate normalization of protein abundance to lysosomes (Table S1G). The identified lysosomal proteins, their quantification between alleles and the precursors used for normalization are provided in Table S2.

Proteins found to be significantly up- or downregulated in hAPOE4 lysosomes relative to hAPOE3 or hAPOE$^{-/-}$controls were tested for enrichment of Gene Ontology (GO Biological Process, Molecular Function and Cellular Component) terms. The over-representation analysis (ORA) was performed using the enricher function from R package clusterProfiler (version 4.2.2) [122]. The gene ontology terms and annotations were obtained from the R annotation package org.Mm.eg.db (version 3.8.2). Non-redundant GO terms were selected by first constructing a term tree based on distances (1-Jaccard Similarity Coefficients of shared genes in GO database) between the significant terms using the R function hclust. The term tree was then cut at a specific level (R function cutree, h = 0.99) to identify clusters of redundant gene sets. For results with multiple significant terms belonging to the same cluster, we selected the most significant term (i.e., minimum adjusted p-value).

Principal component analysis and significance testing were performed using base R (svd and t.test functions respectively). Select protein heatmaps were generated using pheatmap package. Lysosomal protein and gene ontology heatmaps were generated using the complexHeatmap

816 package [123, 124]. Lysosomal overrepresentation analysis was performed by plotting ratios of
817 ratios. The first ratio is the lysosomal distribution coefficient, calculated as the lysosomal protein
818 abundance relative to the whole-cell protein abundance. Proteins that preferentially localize to
819 lysosomes have a high lysosomal distribution coefficient. Conversely, proteins that prefer cytosolic
820 residency have low lysosomal distribution coefficients. To elucidate whether proteins are
821 overrepresented or underrepresented on hAPOE4 lysosomes, we divided the lysosomal distribution
822 coefficients of each protein on hAPOE4 lysosomes by the respective lysosomal distribution
823 coefficient in control cells.
824

825 ***Lgals3bp-GFP Affinity Purification***

826 For each replicate, Neuro-2a cells stably expressing either hAPOE3 or hAPOE4 were seeded onto
827 two 15 cm dishes at a density of 400,000 cells, and allowed to grow for 4 days. Each 15 cm dish
828 was transfected with 60 µg DNA using polyJET (SignaGen #SL100688) to deliver expression
829 vectors for GFP or Lgals3bp-GFP, following the manufacturer's instructions. For each vector, three
830 independent biological replicates were prepared. Media was exchanged the following day, and the
831 cells allowed to recover for another three days before harvesting. The subsequent affinity
832 purification was performed as previously described [31]. For each sample, two 15 cm dishes were
833 each rinsed with PBS and scraped in 500 µL NP40 lysis buffer (50 mM Tris-HCl pH 8.0, 150 mM
834 NaCl, 1 mM EDTA pH 8.0, 0.5% Nonidet P40 Substitute, complete protease inhibitor tablet,
835 phosSTOP phosphatase inhibitor tablet) and combined before freezing on dry ice for 20 minutes.
836 Samples were next thawed in a 37°C water bath for lysis until completely thawed, and frozen at -
837 80°C until GFP immunoprecipitation. Frozen samples were again partially thawed at 37°C, and
838 incubated at 4°C on a tube rotator for 30 minutes. The debris was pelleted by centrifugation (13,000
839 g, 4°C, 15 minutes) and the supernatant transferred to a 96-well deep well plate and kept on ice
840 until GFP immunoprecipitation.
841

842 In addition to lysates, beads and buffers (indicated below) were dispensed into KingFisher 96-well
843 deep-well plates or microplates as appropriate and placed on ice until loaded onto the KingFisher
844 Flex (KFF) Purification System (Thermo Fisher Scientific) for automated processing as follows:
845 GFP-Trap beads (25 µL slurry dispensed in plate 1 only; Cat. #GTMA-10, Chromotek) were
846 equilibrated twice (plates 1,2) with up to 1.0 mL IP Buffer (50 mM Tris–HCl, pH 7.4 at 4 °C, 150
847 mM NaCl, 1 mM EDTA) supplemented with 0.05% NP40 and incubated with (plate 3) 1.0 mL cell
848 lysate for 2 h. Protein-bound beads were washed three times (plates 4-6) with 1.0 mL IP Buffer
849 supplemented with 0.05% NP40 and then once (plate 7) with 1.0 mL IP buffer before elution.
850 Proteins were eluted from beads (plate 8) in 50 µL 0.05% RapiGest in IP Buffer and combined with
851 residual proteins recovered by rinsing beads (plate 9) in 50 µL IP Buffer for sample processing
852 (below). The KFF is operated in a cold room to maintain a 4°C temperature during
853 immunoprecipitation; however, elution and the final bead rinsing steps were performed using a heat
854 block pre-heated to 23°C. Automated protocol steps were performed using the slow mix speed and
855 the following mix times: 30 seconds for equilibration/wash steps, 2 hours for binding, 35 minutes
856 for elution and 2 minutes for the final bead rinse. Five 30 second bead collection times were used
857 at the end of each step before transferring beads to the next plate.
858

859 Proteins from elution and bead rinse steps were combined in a 96-well PCR plate for sample
860 processing as follows: denaturation and reduction at 37°C for 30 m with 2 M urea and 1 mM DTT
861 in 50 mM Tris–HCl pH 8.0, alkylation at room temperature in the dark for 45 m with 3 mM
862 iodoacetamide, and quenching for 10 minutes with 3 mM DTT. Trypsin (0.5 µg/µL; Promega) was
863 added twice (1.0 µL and 0.5 µl) and incubated at 37°C for 4 hours and 2 hours, respectively.
864 Incubations were performed at 37°C in a thermal cycler or at room temperature in a MixMate
865 incubator with shaking at 1,000 rpm. Peptides were acidified with TFA (0.5% final, pH < 2.0) and
866 desalted at room temperature using a BioPureSPE Mini 96-well plate (20 mg PROTO 300 C18;
867 The Nest Group). Briefly, desalting columns were sequentially equilibrated with 0.2 mL 100%
868 methanol; 0.3 mL 80% ACN, 0.1% TFA and 0.3 mL 2% ACN, 0.1% TFA before passing acidified
869 samples through columns twice and subsequently washed with 2% ACN, 0.1% TFA (0.1 mL and
870 0.4 mL) and 0.1% FA (0.4 mL, twice). Peptides were eluted twice with 50% ACN, 0.1% FA (60
871 µL each step) and dried under vacuum centrifugation (CentriVap Concentrator, Labconco). The
872 desalting plate was centrifuged at 2,000 rpm for 2 minutes for initial equilibration steps and 3
873 minutes for all remaining steps. All buffers were prepared with HPLC or LC-MS grade reagents.
874 Within a respective apoE genotype cell line, proteins found to be consistently detected in all
875 Lgals3bp-GFP replicates and significantly enriched over GFP-transfected controls were considered
876 Lgals3bp interaction partners.

877 ***Small molecule-mediated differentiation of human iPSC-derived neurons***

878 The human female apoE4 iPSCs and the isogenic apoE3 iPSCs were previously described [24].
879 Human iPSCs were maintained on Matrigel (Corning #354277) in mTeSR Plus Media (StemCell
880 Technologies #100-0274) and passaged into media supplemented with 10 µM Y-27632 ROCK
881 inhibitor (Tocris #1254) using Accutase (Millipore #scr005). Mixed neurons were generated as
882 reported previously[24], with some modifications. Briefly, iPSCs from 6 100 mm dishes were
883 suspended as single cells in 50 mL KSR medium (80% DMEM #10-566-024, 20% KOSR
884 #10828028, 1X NEAA, 1X GlutaMAX, 0.5X Pen/Strep, 10 µM β-mercaptoethanol) supplemented
885 with 10 µM SB-431542 (Stemgent #04-0010-10), 250 nM LDN-193189 (Stemgent #04-0074), 5
886 µM IWP2 (Millipore #506072), 100 nM SAG (Millipore #566661), and 10 µM ROCK inhibitors
887 and placed into two T75 flasks to form neurospheres. Neurospheres were fed every second day until
888 day in vitro 7 (DIV7), at which point the KSR small molecule supplements were replaced with 100
889 ng/mL FGF8 (Peprotech #100-25), 5 µM IWP2, 100 nM SAG, and 250 nM LDN-193189. At
890 DIV14, neuroepithelium was plated down onto two poly-L-lysine (Sigma #4707)/Laminin
891 (ThermoFisher #23017-015)-coated 100 mm cell culture dishes in N2 media (100% DMEM/F12
892 #11330-032, 0.5X N2 Supplement #17502-048, 1X NEAA, 1X GlutaMAX, 0.5X Pen/Strep)
893 supplemented with 100 ng/mL FGF8 and 100 nM SAG. At DIV21, neuroepithelium was passaged
894 with Accutase, strained through 40 µm filters, counted and centrifuged (200g, 2 min), before they
895 were resuspended in N2/B27 medium (50% DMEM/F12, 50% Neurobasal #21103-049, 0.5X N2
896 Supplement, 0.5X B27 Supplement (ThermoFisher #17504-044), 1X NEAA, 1X GlutaMAX, 0.5X
897 Pen/Strep) supplemented with 10 ng/mL BDNF (Peprotech #450-02) and 10 ng/mL GDNF
898 (Peprotech #450-10) and seeded at a density of 200,000 cells/mL onto PLL/Laminin-coated glass
899 cover-slips. iPSC-derived neurons were fed twice per week by half feeds, and used at DIV49.

900 ***Generation of CRISPRi-repressed iPSC-derived NGN2 neurons***

901 The WTC11 iPSCs with AAVS1-integrated doxycycline-inducible mouse NGN2 and CLYBL-
902 integrated dCas9-BFP-KRAB (CRISPRi) were previously described (CRISPRi-i^{3}N iPSCs)[78].
903 sgRNAs targeting TMED10 ([TGGAGACTCGTTCACCACCGA]), LGALS3BP
904 ([GGCCTGACCACGCTCCATAC]) were cloned into the pMK1334 screening vector and verified
905 by Sanger sequencing. The plasmids were then used to produce lentiviruses, and these used to
906 transduce CRISPRi-i3N iPSCs at 70% MOI. Transduced cells were subsequently selected for my
907 puromycin treatment (1 µg/mL), and following selection cultured in StemFlex Medium (Catalog
908 number: A3349401) on GFR, LDEV-free Matrigel-coated dishes (Corning #356231), diluted 1:100
909 in Knockout DMEM (Thermo Fisher #10829-018). StemFlex was replaced every day, or every
910 other day once 50% confluent, and passaged upon reaching 80-90% confluence using StemPro
911 Accutase (Thermo Fisher #A11105-01). Single-cell iPSCs were always seeded in StemFlex
912 supplemented with 10 nM Y-27632 ROCK inhibitors (Tocris #125410). To generate glutamatergic
913 neurons, iPSCs were passaged and resuspended at 4 x 106 cells per Matrigel-coated T-75 flask in
914 N2 pre-differentiation medium (100% Knockout DMEM/F12 #12660-012, 1X NEAA, 1X N2
915 Supplement #17502-048, 10 ng/mL NT-3 #450-03, 10 ng/mL BDNF# 450-02, 1 µg/mL Laminin
916 #23017-015, and 2 µg/mL Doxycycline hydrochloride #D3447-500MG). During plating and for 24
917 hours only, 10 nM Y-27632 ROCK inhibitor was added to the pre-differentiation medium. After
918 three days at DIV0, cells were passaged with accutase and resuspended at [30,000 cells per well on
919 Corning® BioCoat® Poly-D-Lysine 96-well Black, flat-bottomed plates (354640 in classic
920 neuronal medium (50% DMEM/F12 #11320-033, 50% Neurobasal-A #10888-022, 1X NEAA,
921 0.5X GlutaMAX, 0.5X N2 Supplement, 0.5X B27 Supplement #17504-044, 10 ng/mL NT-3, 10
922 ng/mL BDNF, 1 µg/mL Laminin, and 2 µg/mL Doxycycline hydrochloride. On day 7, half of the
923 medium was replaced with fresh classic neuronal medium without doxycycline. On day 14, half of
924 the medium was removed, and twice this amount of fresh neuronal medium was added back to the
925 cells. The cells were imaged by confocal microscopy on day 21.

926 ***Brain Tissue Samples***

927 Human brain tissue samples were acquired from the Neurodegenerative Disease Brain Bank at the
928 University of California San Francisco. Neuropathological diagnoses were made following
929 consensus diagnostic criteria [125]. Cases were selected based on clinical and neuropathological
930 diagnoses, and stratified based on apoE genotype. All *post-mortem* samples were obtained from
931 patients showing AD pathology at Braak stage 6/Thal stage 5. ApoE3 patients showed an age of
932 onset of 55 and 59 years, and age of death of 75 and 76 years, respectively, while apoE4 patients
933 showed an age of onset of 60 and 53 years, and age of death of 66 and 74, respectively. Frozen
934 human brain tissue samples were dissected from the angular gyrus of apoE3 and apoE4 cases.

935 ***Proximity Ligation Assay***

936 The proximity ligation assay (PLA) was performed following the manufacturer's instructions
937 (Millipore #DUO92101), with minor adaptations to detect lysosomal luminal antigens. For
938 neuronal cultures, DIV49 iPSC-derived neurons were washed twice with calcium-containing PBS,
939 fixed with 4% paraformaldehyde for 30 minutes, and washed once with calcium-containing PBS
940 prior to the assay. For histological samples, paraffin-embedded angular gyrus samples from
941 homozygous apoE3 or apoE4 AD patients were sliced 8 µM thick and dewaxed by baking (65°C,

942 30 min), xylene (10 min) and ethanol deparaffination (2x5 min 100% ethanol, 1 min 100% ethanol,
943 1 min 95% ethanol), peroxidase blocking by 30 min 3% H_2O_2/methanol incubation, and 0.01M
944 citric acid antigen retrieval at 121°C for 5 minutes. All samples were permeabilized and blocked
945 with BB-S for 1 hour at room temperature. Subsequently, the samples were incubated with the
946 following primary antibodies in BB-S at 4°C overnight: mouse anti-LAMP1 (SantaCruz #sc-20011,
947 diluted 1:800), rabbit anti-LAMP1 (CST #9091S, diluted 1:200), rabbit anti-LGALS3BP
948 (ThermoFisher #10281-1-AP, diluted 1:200), and rabbit anti-TMED5 (ThermoFisher #PA5-
949 141055, diluted 1:500). Histological slides were additionally stained with chicken anti-MAP2
950 (abcam #ab5392, diluted 1:10,000).The samples were washed twice in home-made wash buffer A
951 to detect lysosomal antigens (10 mM Tris, 150 mM NaCl, 0.05% Saponin) for 5 minutes, and
952 incubated in a humid chamber with PLA probe solution containing 1X PLUS and MINUS PLA
953 probes against mouse and rabbit primary antibodies for 1 hour at 37°C. The samples were washed
954 twice for 5 minutes with lysosomal wash buffer A, and incubated in 1X ligation solution for 30
955 minutes in a humid chamber at 37°C. The samples were washed twice for 5 minutes with lysosomal
956 wash buffer A, and incubated in 1X amplification solution for 100 minutes in a humid chamber at
957 37°C. The samples were finally washed twice for 10 minutes in 1X wash buffer B (200 mM Tris,
958 100 mM NaCl), once for 1 minute in 0.01X wash buffer B, and mounted in Duolink In Situ
959 Mounting Medium with DAPI on glass slides for confocal microscopy. Images were captured using
960 a confocal laser scanning microscope (Zeiss LSM880) fitted with a Plan-Apochromat 63x/1.4 Oil
961 DIC M27 objective and PMT detector. Nuclei were imaged by excitation at 405 nm and detection
962 between 410-507 nm, with the pinhole set to 1.36 AU. PLA signals were captured using TexasRed
963 excitation/emission settings, with the pinhole set to 1.40 AU. Pixel scaling was set to 70 nm. PLA
964 signals were analyzed in Fiji, drawing region-of-interests around neuronal soma based on PMT and
965 DAPI images, followed by average signal intensity measurements. The experiment was performed
966 in triplicate, using neurons from three different differentiations.

967 ***Validation of lysosomal proteomic dysfunction in the postmortem human***
968 ***neurodegenerative disease brain***

969 Label-free quantitative proteomic data from postmortem human brain tissues were downloaded for
970 the Baltimore Longitudinal Study of Aging (BLSA) at Johns Hopkins University and Banner Sun
971 Health Research Institute (Banner) from the Accelerating Medicines Partnership – Alzheimer
972 Disease (AMP-AD) consortium (https://adknowledgeportal.synapse.org/) [126, 127]. The BLSA
973 samples consisted of 97 samples from the dorsolateral prefrontal cortex (BA9 area) representing 15
974 controls, 15 AsymAD and 20 AD cases [128]. The Banner samples were from prefrontal cortex of
975 30 controls, 28 mild cognitive impairment, 33 AsymAD and 98 confirmed AD cases [91]. The label
976 free quantitation intensities were log2 transformed and assessed for effects from biological
977 covariates (diagnosis, age, gender) and technical variables (batch, brain bank). We used a linear
978 regression model accounting for biological and technical covariates. The final model used was
979 implemented in R version 3.6.1 (R Core Team 2019) as follows:
980 lm(expression ~ diagnosis + age + gender + batch + brain.bank.batch)
981 We evaluated the proteins that were up-regulated proteins in apoE4 lysosomes relative to apoE3 or
982 apoE-deficient lysosomes (apoeE4>apoE3/apoE-deficient). We also evaluated the up-/down-
983 regulated proteins in apoE4 lysosomes only relative to apoE3 lysosomes
984 (apoE4>apoE3|apoE4<apoE3). For these protein sets, we considered their eigenprotein as the first

principal component of their protein expression [129, 130]. We determined if the eigenprotein for apoeE4>apoE3/apoE-deficient or apoeE4>apoE3 were significantly different from disease diagnosis (AD, mild cognitive impairment, AsymAD) versus control using the Wilcoxon rank sum test [131]. Eigenproteins were correlated with apoE4 dosage using Pearson correlation [132].

Statistical analysis

Statistical tests performed are described in the figure legends of their associated graphs. Generally speaking, all data presented was collected from at least three separate technical and biological replicates. In the case of iPSC-derived neurons, one differentiation batch was used as a single biological replicate. The following statistical tests were used, unless otherwise indicated: For comparisons between two conditions (one independent variable), a two-way t-test was performed. For comparisons between multiple conditions across one independent variables, a one-way ANOVA was performed followed *post-hoc* by Bonferroni's multiple comparison test. For comparisons between multiple conditions across multiple independent variables, a two-way ANOVA was performed followed *post-hoc* by Bonferroni's multiple comparison test. All bar graphs present data as the mean ± SEM.

Data and materials availability

All unique and stable reagents, including plasmids and LysoIP cell lines generated in this study, are available from the lead contact without restriction. The proteomic datasets supporting the conclusions of this article is available in the ProteomeXchange Consortium (http://proteomecentral.proteomexchange.org) via the PRIDE partner repository with dataset identifier PXD044942, and can be accessed using the following credentials: Username: reviewer_pxd044942@ebi.ac.uk, Password: XI5oUUKC. The proteomic results and analysis sheets for both LysoIP and APMS experiments are also listed in supplemental tables S1 and S2, respectively. The human brain results published here are in whole or in part based on data obtained from the AMP-AD Knowledge Portal (https://adknowledgeportal.synapse.org/).

Acknowledgments

We thank Robert W. Mahley for helpful discussions. We thank Ken Nakamura and Huihui Li for sharing the mtKeima plasmid, and Monther Abu-Remaileh and Ali Ghoochani for sharing LysoIP plasmids. We also thank Margaret Soucheray and Holli Deval for lab organization, Ben Polacco for bioinformatic support, and the rest of the Krogan laboratory for helpful discussions around the data presented herein. We thank the Gladstone Histology & Light Microscopy Core for supporting all confocal microscopy experiments. Human tissue samples were obtained with the help of Lea Grinberg, Wing Hung Lee, and Tia LaMore from the Neurodegenerative Disease Brain Bank, UCSF, supported by grant number P30 AG062422 (Alzheimer's Disease Research Center). BLSA data were generated from postmortem brain tissue collected through the National Institute on Aging's Baltimore Longitudinal Study of Aging and provided by Dr. Levey from Emory University. Banner data were provided by Dr. Levey from Emory University. A portion of these data were generated from samples collected through the Sun Health Research Institute Brain and Body Donation Program of Sun City, Arizona.

Funding

National Institutes of Health grant R01AG059751 (NJK, DLS)
National Institutes of Health grant U54NS123746 (DLS)
National Institutes of Health grant R01AG071697 (YH)
National Institute of Neurological Disorders and Stroke grant R25NS065723 (TSC)
National Institute of Neurological Disorders and Stroke grant U24 NS072026 (Brain and Body Donation Program)
National Institute on Aging grant P30 AG19610 (Arizona Alzheimer's Disease Core Center)
Arizona Department of Health Services contract 211002 (Arizona Alzheimer's Research Center)
Arizona Biomedical Research Commission contracts 4001, 0011, 05-901, 1001 (Arizona Parkinson's Disease Consortium)
Michael J. Fox Foundation for Parkinson's Research (TSC)
California Institute of Regenerative Medicine Fellowship (EKK)
Gladstone Institutes PUMAS Program (AM)

Author contributions

Conceptualization: EKK, ZC, DLS. **Data curation:** JM, LV-B, TSC. **Formal analysis:** EKK, JM, AM, AW, LV-B, TSC. **Funding acquisition:** MK, YH, NJK, DLS, TSC. **Investigation:** EKK, JM, LV-B, AM, AW, ES, GMJ, AR, EL, AA, AZ. **Methodology:** EKK, JM, GMJ, AR, EL, AZ, TSC, YH, DLS. **Project administration:** DLS. **Resources:** MK, YH, NJK, DLS. **Software:** JM. **Supervision**: EKK, TSC, MK, YH, NJK, DLS. **Validation:** EKK, JM. **Visualization:** EKK, JM, LV-B, TSC. **Writing – original draft:** EKK, DLS. **Writing – review & editing:** EKK, JM, LV-B, GMJ, TSC, YH, NJK, DLS.

Competing interests

Yadong Huang is a co-founder and scientific advisory board member of GABAeron. The Krogan Laboratory has received research support from Vir Biotechnology, F. Hoffmann-La Roche, and Rezo Therapeutics. Nevan J. Krogan has previously held financially compensated consulting agreements with the Icahn School of Medicine at Mount Sinai, New York, and Twist Bioscience Corp. He currently has financially compensated consulting agreements with Maze Therapeutics, Interline Therapeutics, Rezo Therapeutics, and GEn1E Lifesciences, Inc. He is on the Board of Directors of Rezo Therapeutics and is a shareholder in Tenaya Therapeutics, Maze Therapeutics, Rezo Therapeutics, and Interline Therapeutics. Danielle L. Swaney has financially compensated consulting agreements with Maze Therapeutics and Rezo Therapeutics. The authors have no additional financial interests. The other authors declare no competing interests.

References

1. The World Health Organization. (2021). World failing to address dementia challenge. WHO News. https://www.who.int/news/item/02-09-2021-world-failing-to-address-dementia-challenge.
2. Ballard, C., Gauthier, S., Corbett, A., Brayne, C., Aarsland, D., and Jones, E. (2011). Alzheimer's disease. Lancet *377*, 1019–1031. 10.1016/S0140.

1067 3. Silva, M.V.F., Loures, C.D.M.G., Alves, L.C.V., De Souza, L.C., Borges, K.B.G., and Carvalho, M.D.G.
1068 (2019). Alzheimer's disease: Risk factors and potentially protective measures. J Biomed Sci *26*. 10.1186/s12929-019-
1069 0524-y.
1070 4. Yamazaki, Y., Painter, M.M., Bu, G., and Kanekiyo, T. (2016). Apolipoprotein E as a Therapeutic Target in
1071 Alzheimer's Disease: A Review of Basic Research and Clinical Evidence. CNS Drugs *30*, 773–789. 10.1007/s40263-
1072 016-0361-4.
1073 5. Corder, E.H., Saunders, A.M., Gaskell, P.C., Pericak-Vance, M.A., Strittmatter, W.J., Roses, A.D., Haines,
1074 J.L., and Pericak-Vance, M.A. (1993). Gene Dose of Apolipoprotein E Type 4 Allele and the Risk of Alzheimer's
1075 Disease in Late Onset Families. Science (1979) *261*, 921–923.
1076 6. Michaelson, D.M. (2014). APOE ε4: The most prevalent yet understudied risk factor for Alzheimer's
1077 disease. Preprint at Elsevier Inc., 10.1016/j.jalz.2014.06.015 10.1016/j.jalz.2014.06.015.
1078 7. Langella, S., Barksdale, N.G., Vasquez, D., Aguillon, D., Chen, Y., Su, Y., Acosta-Baena, N., Acosta-Uribe,
1079 J., Baena, A.Y., Garcia-Ospina, G., et al. (2023). Effect of apolipoprotein genotype and educational attainment on
1080 cognitive function in autosomal dominant Alzheimer's disease. Nat Commun *14*, 5120. 10.1038/s41467-023-40775-
1081 z.
1082 8. Levi, O., Jongen-Relo, A.L., Feldon, J., Roses, A.D., and Michaelson, D.M. (2003). ApoE4 impairs
1083 hippocampal plasticity isoform-specifically and blocks the environmental stimulation of synaptogenesis and memory.
1084 Neurobiol Dis *13*, 273–282. 10.1016/S0969-9961(03)00045-7.
1085 9. Teter, B. (2004). ApoE-Dependent Plasticity in Alzheimer's Disease. J Mol Neurosci *23*, 167–179.
1086 10. Levi, O., Jongen-Relo, A.L., Feldon, J., and Michaelson, D.M. (2005). Brain area- and isoform-specific
1087 inhibition of synaptic plasticity by apoE4. J Neurol Sci *229–230*, 241–248. 10.1016/j.jns.2004.11.035.
1088 11. Chen, Y., Durakoglugil, M.S., Xian, X., and Herz, J. (2010). ApoE4 reduces glutamate receptor function and
1089 synaptic plasticity by selectively impairing ApoE receptor recycling. Proc Natl Acad Sci U S A *107*, 12011–12016.
1090 10.1073/pnas.0914984107.
1091 12. Koutsodendris, N., Blumenfeld, J., Agrawal, A., Traglia, M., Grone, B., Zilberter, M., Yip, O., Rao, A.,
1092 Nelson, M.R., Hao, Y., et al. (2023). Neuronal APOE4 removal protects against tau-mediated gliosis,
1093 neurodegeneration and myelin deficits. Nat Aging. 10.1038/s43587-023-00368-3.
1094 13. Mishra, S., Blazey, T.M., Holtzman, D.M., Cruchaga, C., Su, Y., Morris, J.C., Benzinger, T.L.S., and
1095 Gordon, B.A. (2018). Longitudinal brain imaging in preclinical Alzheimer disease: Impact of APOE ϵ4 genotype.
1096 Brain *141*, 1828–1839. 10.1093/brain/awy103.
1097 14. Raber, J., Wong, D., Buttini, M., Orth, M., Bellosta, S., Pitas, R.E., Mahley, R.W., and Mucke, L. (1998).
1098 Isoform-specific effects of human apolipoprotein E on brain function revealed in ApoE knockout mice: Increased
1099 susceptibility of females. Proc Natl Acad Sci U S A *95*, 10914–10919. 10.1073/pnas.95.18.10914.
1100 15. Hartman, R.E., Wozniak, D.F., Nardi, A., Olney, J.W., Sartorius, L., and Holtzman, D.M. (2001).
1101 Behavioral phenotyping of GFAP-ApoE3 and -ApoE4 transgenic mice: ApoE4 mice show profound working
1102 memory impairments in the absence of Alzheimer's-like neuropathology. Exp Neurol *170*, 326–344.
1103 10.1006/exnr.2001.7715.
1104 16. Grootendorst, J., Bour, A., Vogel, E., Kelche, C., Sullivan, P.M., Dodart, J.C., Bales, K., and Mathis, C.
1105 (2005). Human apoE targeted replacement mouse lines: h-apoE4 and h-apoE3 mice differ on spatial memory
1106 performance and avoidance behavior. Behavioural Brain Research *159*, 1–14. 10.1016/j.bbr.2004.09.019.
1107 17. Tong, L.M., Djukic, B., Arnold, C., Gillespie, A.K., Yoon, S.Y., Wang, M.M., Zhang, O., Knoferle, J.,
1108 Rubenstein, J.L.R., Alvarez-Buylla, A., et al. (2014). Inhibitory interneuron progenitor transplantation restores
1109 normal learning and memory in ApoE4 knock-in mice without or with Aβ accumulation. Journal of Neuroscience *34*,
1110 9506–9515. 10.1523/JNEUROSCI.0693-14.2014.
1111 18. Yamazaki, Y., Liu, C.C., Yamazaki, A., Shue, F., Martens, Y.A., Chen, Y., Qiao, W., Kurti, A., Oue, H.,
1112 Ren, Y., et al. (2021). Vascular ApoE4 Impairs Behavior by Modulating Gliovascular Function. Neuron *109*, 438-
1113 447.e6. 10.1016/j.neuron.2020.11.019.
1114 19. Najm, R., Zalocusky, K.A., Zilberter, M., Yoon, S.Y., Hao, Y., Koutsodendris, N., Nelson, M., Rao, A.,
1115 Taubes, A., Jones, E.A., et al. (2020). In Vivo Chimeric Alzheimer's Disease Modeling of Apolipoprotein E4
1116 Toxicity in Human Neurons. Cell Rep *32*, 107962. 10.1016/j.celrep.2020.107962.
1117 20. Lin, Y.T., Seo, J., Gao, F., Feldman, H.M., Wen, H.L., Penney, J., Cam, H.P., Gjoneska, E., Raja, W.K.,
1118 Cheng, J., et al. (2018). APOE4 Causes Widespread Molecular and Cellular Alterations Associated with Alzheimer's

1119 Disease Phenotypes in Human iPSC-Derived Brain Cell Types. Neuron *98*, 1141-1154.e7.
1120 10.1016/j.neuron.2018.05.008.
1121 21. Wang, C., Najm, R., Xu, Q., Jeong, D.E., Walker, D., Balestra, M.E., Yoon, S.Y., Yuan, H., Li, G., Miller,
1122 Z.A., et al. (2018). Gain of toxic apolipoprotein E4 effects in human iPSC-derived neurons is ameliorated by a small-
1123 molecule structure corrector. Nat Med *24*, 647–657. 10.1038/s41591-018-0004-z.
1124 22. Zalocusky, K.A., Najm, R., Taubes, A.L., Hao, Y., Yoon, S.Y., Koutsodendris, N., Nelson, M.R., Rao, A.,
1125 Bennett, D.A., Bant, J., et al. (2021). Neuronal ApoE upregulates MHC-I expression to drive selective
1126 neurodegeneration in Alzheimer's disease. Nat Neurosci *24*, 786–798. 10.1038/s41593-021-00851-3.
1127 23. Prasad, H., and Rao, R. (2018). Amyloid clearance defect in ApoE4 astrocytes is reversed by epigenetic
1128 correction of endosomal pH. Proc Natl Acad Sci U S A *115*, E6640–E6649. 10.1073/pnas.1801612115.
1129 24. Blanchard, J.W., Akay, L.A., Davila-Velderrain, J., von Maydell, D., Mathys, H., Davidson, S.M.,
1130 Effenberger, A., Chen, C.Y., Maner-Smith, K., Hajjar, I., et al. (2022). APOE4 impairs myelination via cholesterol
1131 dysregulation in oligodendrocytes. Nature *611*, 769–779. 10.1038/s41586-022-05439-w.
1132 25. Nathan, B.P., Chang, K.C., Bellosta, S., Brisch, E., Ge, N., Mahley, R.W., and Pitas, R.E. (1995). The
1133 inhibitory effect of apolipoprotein E4 on neurite outgrowth is associated with microtubule depolymerization. Journal
1134 of Biological Chemistry *270*, 19791–19799. 10.1074/jbc.270.34.19791.
1135 26. Muth, C., Hartmann, A., Sepulveda-Falla, D., Glatzel, M., and Krasemann, S. (2019). Phagocytosis of
1136 apoptotic cells is specifically upregulated in apoe4 expressing microglia in vitro. Front Cell Neurosci *13*.
1137 10.3389/fncel.2019.00181.
1138 27. Mahley, R.W., and Huang, Y. (2006). Apolipoprotein (apo) E4 and Alzheimer's disease: Unique
1139 conformational and biophysical properties of apoE4 can modulate neuropathology. Preprint, 10.1111/j.1600-
1140 0404.2006.00679.x 10.1111/j.1600-0404.2006.00679.x.
1141 28. Cakir, Z., Lord, S.J., Zhou, Y., Jang, G.M., Polacco, B.J., Eckhardt, M., Jimenez-Morales, D., Newton,
1142 B.W., Orr, A.L., Johnson, J.R., et al. (2023). Quantitative Proteomic Analysis Reveals apoE4-Dependent
1143 Phosphorylation of the Actin-Regulating Protein VASP. Mol Cell Proteomics *22*, 100541.
1144 10.1016/j.mcpro.2023.100541.
1145 29. Castellano, J.M., Kim, J., Stewart, F.R., Jiang, H., Demattos, R.B., Patterson, B.W., Fagan, A.M., Morris,
1146 J.C., Mawuenyega, K.G., Cruchaga, C., et al. (2011). Human apoE Isoforms Differentially Regulate Brain Amyloid-b
1147 Peptide Clearance.
1148 30. Deane, R., Sagare, A., Hamm, K., Parisi, M., Lane, S., Finn, M.B., Holtzman, D.M., and Zlokovic, B. V.
1149 (2008). apoE isoform-specific disruption of amyloid β peptide clearance from mouse brain. Journal of Clinical
1150 Investigation *118*, 4002–4013. 10.1172/JCI36663.
1151 31. Tzioras, M., Davies, C., Newman, A., Jackson, R., and Spires-Jones, T. (2019). APOE at the interface of
1152 inflammation, neurodegeneration and pathological protein spread in Alzheimer's disease. Preprint at Blackwell
1153 Publishing Ltd, 10.1111/nan.12529 10.1111/nan.12529.
1154 32. Schmukler, E., Solomon, S., Simonovitch, S., Goldshmit, Y., Wolfson, E., Michaelson, D.M., and Pinkas-
1155 Kramarski, R. (2020). Altered mitochondrial dynamics and function in APOE4-expressing astrocytes. Cell Death Dis
1156 *11*. 10.1038/s41419-020-02776-4.
1157 33. Simonovitch, S., Schmukler, E., Masliah, E., Pinkas-Kramarski, R., and Michaelson, D.M. (2019). The
1158 Effects of APOE4 on Mitochondrial Dynamics and Proteins in vivo. Journal of Alzheimer's Disease *70*, 861–875.
1159 10.3233/JAD-190074.
1160 34. Orr, A.L., Kim, C., Jimenez-Morales, D., Newton, B.W., Johnson, J.R., Krogan, N.J., Swaney, D.L., and
1161 Mahley, R.W. (2019). Neuronal Apolipoprotein E4 Expression Results in Proteome-Wide Alterations and
1162 Compromises Bioenergetic Capacity by Disrupting Mitochondrial Function. Journal of Alzheimer's Disease *68*, 991–
1163 1011. 10.3233/JAD-181184.
1164 35. Xian, X., Pohlkamp, T., Durakoglugil, M.S., Wong, C.H., Rgen, J., Beck, K., Lane-Donovan, C., Plattner,
1165 F., and Herz, J. (2018). Reversal of ApoE4-induced recycling block as a novel prevention approach for Alzheimer's
1166 disease. 10.7554/eLife.40048.001.
1167 36. Rawat, V., Wang, S., Sima, J., Bar, R., Liraz, O., Gundimeda, U., Parekh, T., Chan, J., Johansson, J.O.,
1168 Tang, C., et al. (2019). ApoE4 Alters ABCA1 membrane trafficking in astrocytes. Journal of Neuroscience *39*, 9611–
1169 9622. 10.1523/JNEUROSCI.1400-19.2019.

1170 37. Narayan, P., Sienski, G., Bonner, J.M., Lin, Y.T., Seo, J., Baru, V., Haque, A., Milo, B., Akay, L.A.,
1171 Graziosi, A., et al. (2020). PICALM Rescues Endocytic Defects Caused by the Alzheimer's Disease Risk Factor
1172 APOE4. Cell Rep *33*. 10.1016/j.celrep.2020.108224.
1173 38. Nuriel, T., Peng, K.Y., Ashok, A., Dillman, A.A., Figueroa, H.Y., Apuzzo, J., Ambat, J., Levy, E., Cookson,
1174 M.R., Mathews, P.M., et al. (2017). The endosomal-lysosomal pathway is dysregulated by APOE4 expression in
1175 vivo. Front Neurosci *11*, 1–12. 10.3389/fnins.2017.00702.
1176 39. Nakamura, T., Watanabe, A., Fujino, T., Hosono, T., and Michikawa, M. (2009). Apolipoprotein E4 (1-272)
1177 fragment is associated with mitochondrial proteins and affects mitochondrial function in neuronal cells. Mol
1178 Neurodegener *4*, 1–11. 10.1186/1750-1326-4-35.
1179 40. Chen, H.K., Ji, Z.S., Dodson, S.E., Miranda, R.D., Rosenblum, C.I., Reynolds, I.J., Freedman, S.B.,
1180 Weisgraber, K.H., Huang, Y., and Mahley, R.W. (2011). Apolipoprotein E4 domain interaction mediates detrimental
1181 effects on mitochondria and is a potential therapeutic target for alzheimer disease. Journal of Biological Chemistry
1182 *286*, 5215–5221. 10.1074/jbc.M110.151084.
1183 41. Basit, F., van Oppen, L.M.P.E., Schöckel, L., Bossenbroek, H.M., van Emst-De Vries, S.E., Hermeling,
1184 J.C.W., Grefte, S., Kopitz, C., Heroult, M., Willems, P.H.G.M., et al. (2017). Mitochondrial complex i inhibition
1185 triggers a mitophagy-dependent ROS increase leading to necroptosis and ferroptosis in melanoma cells. Cell Death
1186 Dis *8*. 10.1038/cddis.2017.133.
1187 42. Palikaras, K., Princz, A., and Tavernarakis, N. (2019). Mitophagy modulators. In Encyclopedia of
1188 Biomedical Gerontology (Elsevier Inc.), pp. 433–446. 10.1016/B978-0-12-801238-3.62137-2.
1189 43. Karch, C.M., and Goate, A.M. (2015). Alzheimer's Disease Risk Genes and Mechanisms of Disease
1190 Pathogenesis. Biol Psychiatry *77*, 43–51. 10.1016/j.biopsych.2014.05.006.
1191 44. Hung, C.O.Y., and Livesey, F.J. (2018). Altered gamma-Secretase Processing of APP Disrupts Lysosome
1192 and Autophagosome Function in Monogenic Alzheimer's Disease. Cell Rep *25*, 3647–3660.
1193 10.1016/j.celrep.2018.11.095.
1194 45. Gao, S., Casey, A.E., Sargeant, T.J., and Mäkinen, V.P. (2018). Genetic variation within endolysosomal
1195 system is associated with late-onset Alzheimer's disease. Brain *141*, 2711–2720. 10.1093/brain/awy197.
1196 46. Zhang, L., Sheng, R., and Qin, Z. (2009). The lysosome and neurodegenerative diseases. Acta Biochim
1197 Biophys Sin *41*, 437–445. 10.1093/abbs/gmp031.Review.
1198 47. Leeman, D.S., Hebestreit, K., Ruetz, T., Webb, A.E., McKay, A., Pollina, E.A., Dulken, B.W., Zhao, X.,
1199 Yeo, R.W., Ho, T.T., et al. (2018). Lysosome activation clears aggregates and enhances quiescent neural stem cell
1200 activation during aging. Science (1979) *359*, 1277–1283. 10.1126/science.aag3048.
1201 48. Platt, F.M., D'Azzo, A., Davidson, B.L., Neufeld, E.F., and Tifft, C.J. (2018). Lysosomal storage diseases.
1202 Nat Rev Dis Primers *4*, 27. 10.1038/s41572-018-0025-4.
1203 49. Krogsaeter, E., Scotto, A., and Grimm, C. (2022). TRPMLs and TPCs: Targets for lysosomal storage and
1204 neurodegenerative disease therapy? Cell Calcium *103*, 102553. 10.1016/j.ceca.2022.102553.
1205 50. Bahr, B.A., and Bendiske, J. (2002). The neuropathogenic contributions of lysosomal dysfunction. J
1206 Neurochem *83*, 481–489.
1207 51. Keilani, S., Lun, Y., Stevens, A.C., Williams, H.N., Sjoberg, E.R., Khanna, R., Valenzano, K.J., Checler, F.,
1208 Buxbaum, J.D., Yanagisawa, K., et al. (2012). Lysosomal dysfunction in a mouse model of sandhoff disease leads to
1209 accumulation of ganglioside-bound amyloid-β peptide. Journal of Neuroscience *32*, 5223–5236.
1210 10.1523/JNEUROSCI.4860-11.2012.
1211 52. Guan, J., Mishra, S., Qiu, Y., Shi, J., Trudeau, K., Las, G., Liesa, M., Shirihai, O.S., Connors, L.H., Seldin,
1212 D.C., et al. (2014). Lysosomal dysfunction and impaired autophagy underlie the pathogenesis of amyloidogenic light
1213 chain-mediated cardiotoxicity. EMBO Mol Med *6*, 1493–1507. 10.15252/emmm.201404190.
1214 53. Laili, I.N., Nasir, M.H.M., Jufri, N.F., Ibrahim, F.W., and Hamid, A. (2023). Lysosomal dysfunction
1215 induced cytosolic vacuolation and increased intracellular amyloid-beta 42 (Aβ42) in human brain endothelial cells
1216 (HBEC-5i). Biomedicine and Pharmacotherapy *161*. 10.1016/j.biopha.2023.114501.
1217 54. Li, J., Kanekiyo, T., Shinohara, M., Zhang, Y., LaDu, M.J., Xu, H., and Bu, G. (2012). Differential
1218 regulation of amyloid-β endocytic trafficking and lysosomal degradation by apolipoprotein E isoforms. Journal of
1219 Biological Chemistry *287*, 44593–44601. 10.1074/jbc.M112.420224.
1220 55. Sannerud, R., Esselens, C., Ejsmont, P., Mattera, R., Rochin, L., Tharkeshwar, A.K., De Baets, G., De
1221 wever, V., Habets, R., Baert, V., et al. (2016). Restricted Location of PSEN2/gamma-Secretase Determines Substrate
1222 Specificity and Generates an Intracellular Abeta Pool. Cell *166*, 193–208. 10.1016/j.cell.2016.05.020.

1223 56. Lee, J.-H., Yu, W.H., Kumar, A., Lee, S., Mohan, P.S., Peterhoff, C.M., Wolfe, D.M., Martinez-vicente, M.,
1224 Massey, A.C., Sovak, G., et al. (2010). Lysosomal Proteolysis and Autophagy Require Presenilin 1 and Are
1225 Disrupted by Alzheimer-Related PS1 Mutations. Cell *141*, 1146–1158. 10.1016/j.cell.2010.05.008.
1226 57. Fote, G.M., Geller, N.R., Efstathiou, N.E., Hendricks, N., Vavvas, D.G., Reidling, J.C., Thompson, L.M.,
1227 and Steffan, J.S. (2022). Isoform-dependent lysosomal degradation and internalization of apolipoprotein E requires
1228 autophagy proteins. J Cell Sci *135*. 10.1242/jcs.258687.
1229 58. Harris, F.M., Tesseur, I., Brecht, W.J., Xu, Q., Mullendorff, K., Chang, S., Wyss-Coray, T., Mahley, R.W.,
1230 and Huang, Y. (2004). Astroglial regulation of apolipoprotein E expression in neuronal cells: Implications for
1231 Alzheimer's disease. Journal of Biological Chemistry *279*, 3862–3868. 10.1074/jbc.M309475200.
1232 59. Morgan, A.J., Platt, F.M., Lloyd-Evans, E., and Galione, A. (2011). Molecular mechanisms of
1233 endolysosomal Ca 2+ signalling in health and disease. Preprint, 10.1042/BJ20110949 10.1042/BJ20110949.
1234 60. Li, M., Zhang, C.S., Zong, Y., Feng, J.W., Ma, T., Hu, M., Lin, Z., Li, X., Xie, C., Wu, Y., et al. (2019).
1235 Transient Receptor Potential V Channels Are Essential for Glucose Sensing by Aldolase and AMPK. Cell Metab *30*,
1236 508-524.e12. 10.1016/j.cmet.2019.05.018.
1237 61. Yuan, Y., Kilpatrick, B.S., Gerndt, S., Bracher, F., Grimm, C., Schapira, A.H., and Patel, S. (2021). The
1238 lysosomotrope GPN mobilises Ca2+ from acidic organelles. J Cell Sci *134*. 10.1242/jcs.256578.
1239 62. Abu-Remaileh, M., Wyant, G.A., Kim, C., Laqtom, N.N., Abbasi, M., Chan, S.H., Freinkman, E., and
1240 Sabatina, D.M. (2017). Lysosomal metabolomics reveals V-ATPase- and mTOR-dependent mechanisms for the
1241 efflux of amino acids from lysosomes. Science (1979) *358*, 4.
1242 63. Zavodszky, E., and Hegde, R.S. (2019). Misfolded GPI-anchored proteins are escorted through the secretory
1243 pathway by ER-derived factors. Elife *8*, e46740.
1244 64. Pires, G., McElligott, S., Drusinsky, S., Halliday, G., Potier, M., Wisniewski, T., and Drummond, E. (2019).
1245 Secernin-1 is a novel phosphorylated tau binding protein that accumulates in Alzheimer's disease and not in other
1246 tauopathies. Acta Neuropathol Commun *7*, 1–17.
1247 65. Singh, M.K., Richter, S., Beckmann, H., Kientz, M., Nielsen, M., Kno, C., Stierhof, D., Anders, N., Fa, F.,
1248 Thomann, A., et al. (2018). A single class of ARF GTPase acativated by several pathway-specific ARF-GEFs
1249 regulates essential membrane traffic in Arabidopsis. PLoS Genet *14*, 1–36. 10.1371/journal.pgen.1007795.
1250 66. Knoferle, J., Yoon, S.Y., Walker, D., Leung, L., Gillespie, A.K., Tong, L.M., Bien-Ly, N., and Huang, Y.
1251 (2014). Apolipoprotein E4 produced in GABAergic interneurons causes learning and memory deficits in mice.
1252 Journal of Neuroscience *34*, 14069–14078. 10.1523/JNEUROSCI.2281-14.2014.
1253 67. Koutsodendris, N., Nelson, M.R., Rao, A., and Huang, Y. (2021). Apolipoprotein E and Alzheimer's
1254 Disease: Findings, Hypotheses, and Potential Mechanisms. Annu Rev Pathol, 73–99. 10.1146/annurev-pathmechdis-
1255 030421-112756.
1256 68. Ji, Z.S., Dennis Miranda, R., Newhouse, Y.M., Weisgraber, K.H., Huang, Y., and Mahley, R.W. (2002).
1257 Apolipoprotein E4 potentiates amyloid β peptide-induced lysosomal leakage and apoptosis in neuronal cells. Journal
1258 of Biological Chemistry *277*, 21821–21828. 10.1074/jbc.M112109200.
1259 69. Harris, F.M., Brecht, W.J., Xu, Q., Mahley, R.W., and Huang, Y. (2004). Increased tau phosphorylation in
1260 apolipoprotein E4 transgenic mice is associated with activation of extracellular signal-regulated kinase. Journal of
1261 Biological Chemistry *279*, 44795–44801. 10.1074/jbc.M408127200.
1262 70. Brecht, W.J., Harris, F.M., Chang, S., Tesseur, I., Yu, G.Q., Xu, Q., Fish, J.D., Wyss-Coray, T., Buttini, M.,
1263 Mucke, L., et al. (2004). Neuron-Specific Apolipoprotein E4 Proteolysis Is Associated with Increased Tau
1264 Phosphorylation in Brains of Transgenic Mice. Journal of Neuroscience *24*, 2527–2534. 10.1523/JNEUROSCI.4315-
1265 03.2004.
1266 71. Carosi, J.M., Hein, L.K., van den Hurk, M., Adams, R., Milky, B., Singh, S., Bardy, C., Denton, D., Kumar,
1267 S., and Sargeant, T.J. (2021). Retromer regulates the lysosomal clearance of MAPT/tau. Autophagy *17*, 2217–2237.
1268 10.1080/15548627.2020.1821545.
1269 72. Xu, Y., Du, S., Marsh, J.A., Horie, K., Sato, C., Ballabio, A., Karch, C.M., Holtzman, D.M., and Zheng, H.
1270 (2021). TFEB regulates lysosomal exocytosis of tau and its loss of function exacerbates tau pathology and spreading.
1271 Mol Psychiatry *26*, 5925–5939. 10.1038/s41380-020-0738-0.
1272 73. Lee, M.J., Lee, J.H., and Rubinsztein, D.C. (2013). Tau degradation: The ubiquitin-proteasome system
1273 versus the autophagy-lysosome system. Preprint, 10.1016/j.pneurobio.2013.03.001 10.1016/j.pneurobio.2013.03.001.

1274 74. Hamano, T., Gendron, T.F., Causevic, E., Yen, S.H., Lin, W.L., Isidoro, C., Deture, M., and Ko, L.W.
1275 (2008). Autophagic-lysosomal perturbation enhances tau aggregation in transfectants with induced wild-type tau
1276 expression. European Journal of Neuroscience *27*, 1119–1130. 10.1111/j.1460-9568.2008.06084.x.
1277 75. Khurana, V., Elson-Schwab, I., Fulga, T.A., Sharp, K.A., Loewen, C.A., Mulkearns, E., Tyynelä, J.,
1278 Scherzer, C.R., and Feany, M.B. (2010). Lysosomal dysfunction promotes cleavage and neurotoxicity of tau in vivo.
1279 PLoS Genet *6*, 1–11. 10.1371/journal.pgen.1001026.
1280 76. Wang, Y., Martinez-Vicente, M., Krüger, U., Kaushik, S., Wong, E., Mandelkow, E.M., Cuervo, A.M., and
1281 Mandelkow, E. (2009). Tau fragmentation, aggregation and clearance: The dual role of lysosomal processing. Hum
1282 Mol Genet *18*, 4153–4170. 10.1093/hmg/ddp367.
1283 77. Piovesana, E., Magrin, C., Ente, M.S., Cantonale, O., Bellotto, M., Molinari, M., and Paganetti, P. (2023).
1284 Tau Accumulation in Degradative Organelles is Associated to Lysosomal Stress. Research Square Preprint.
1285 10.21203/rs.3.rs-2972040/v1.
1286 78. Sampognaro, P.J., Arya, S., Knudsen, G.M., Gunderson, E.L., Sandoval-Perez, A., Hodul, M., Bowles, K.,
1287 Craik, C.S., Jacobson, M.P., and Kao, A.W. (2023). Mutations in α-synuclein, TDP-43 and tau prolong protein half-
1288 life through diminished degradation by lysosomal proteases. Mol Neurodegener *18*. 10.1186/s13024-023-00621-8.
1289 79. Rose, K., Jepson, T., Shukla, S., Maya-Romero, A., Kampmann, M., Xu, K., and Hurley, J.H. (2023). Tau
1290 fibrils induce nanoscale membrane damage and nucleate cytosolic tau at lysosomes. biorXiv Preprint.
1291 https://doi.org/10.1101/2023.08.28.555157.
1292 80. Tian, R., Gachechiladze, M.A., Ludwig, C.H., Laurie, M.T., Hong, J.Y., Nathaniel, D., Prabhu, A. V.,
1293 Fernandopulle, M.S., Patel, R., Abshari, M., et al. (2019). CRISPR Interference-Based Platform for Multimodal
1294 Genetic Screens in Human iPSC-Derived Neurons. Neuron *104*, 239-255.e12. 10.1016/j.neuron.2019.07.014.
1295 81. Tian, R., Abarientos, A., Hong, J., Hashemi, S.H., Yan, R., Dräger, N., Leng, K., Nalls, M.A., Singleton,
1296 A.B., Xu, K., et al. (2021). Genome-wide CRISPRi/a screens in human neurons link lysosomal failure to ferroptosis.
1297 Nat Neurosci *24*, 1020–1034. 10.1038/s41593-021-00862-0.
1298 82. Swarup, V., Chang, T.S., Duong, D.M., Dammer, E.B., Dai, J., Lah, J.J., Johnson, E.C.B., Seyfried, N.T.,
1299 Levey, A.I., and Geschwind, D.H. (2020). Identification of Conserved Proteomic Networks in Neurodegenerative
1300 Dementia. Cell Rep *31*. 10.1016/j.celrep.2020.107807.
1301 83. Alam, M.S. (2018). Proximity Ligation Assay (PLA). Curr Protoc Immunol *123*. 10.1002/cpim.58.
1302 84. Barral, D.C., Staiano, L., Guimas Almeida, C., Cutler, D.F., Eden, E.R., Futter, C.E., Galione, A., Marques,
1303 A.R.A., Medina, D.L., Napolitano, G., et al. (2022). Current methods to analyze lysosome morphology, positioning,
1304 motility and function. Preprint at John Wiley and Sons Inc, 10.1111/tra.12839 10.1111/tra.12839.
1305 85. de Araujo, M.E.G., Liebscher, G., Hess, M.W., and Huber, L.A. (2020). Lysosomal size matters. Preprint at
1306 Blackwell Munksgaard, 10.1111/tra.12714 10.1111/tra.12714.
1307 86. Fogeron, M.L., Müller, H., Schade, S., Dreher, F., Lehmann, V., Kühnel, A., Scholz, A.K., Kashofer, K.,
1308 Zerck, A., Fauler, B., et al. (2013). LGALS3BP regulates centriole biogenesis and centrosome hypertrophy in cancer
1309 cells. Nat Commun *4*. 10.1038/ncomms2517.
1310 87. Costa, J., Pronto-Laborinho, A., Pinto, S., Gromicho, M., Bonucci, S., Tranfield, E., Correia, C., Alexandre,
1311 B.M., and de Carvalho, M. (2020). Investigating LGALS3BP/90 K glycoprotein in the cerebrospinal fluid of patients
1312 with neurological diseases. Sci Rep *10*, 1–9. 10.1038/s41598-020-62592-w.
1313 88. Kyrousi, C., O'Neill, A.C., Brazovskaja, A., He, Z., Kielkowski, P., Coquand, L., Di Giaimo, R., D' Andrea,
1314 P., Belka, A., Forero Echeverry, A., et al. (2021). Extracellular LGALS3BP regulates neural progenitor position and
1315 relates to human cortical complexity. Nat Commun *12*. 10.1038/s41467-021-26447-w.
1316 89. Song, Y., Wang, M., Tong, H., Tan, Y., Hu, X., Wang, K., and Wan, X. (2021). Plasma exosomes from
1317 endometrial cancer patients contain LGALS3BP to promote endometrial cancer progression. Oncogene *40*, 633–646.
1318 10.1038/s41388-020-01555-x.
1319 90. Yap, N.V.L., Whelan, F.J., Bowdish, D.M.E., and Golding, G.B. (2015). The evolution of the scavenger
1320 receptor cysteine-rich domain of the class A scavenger receptors. Front Immunol *6*. 10.3389/fimmu.2015.00342.
1321 91. Stogios, P.J., and Privé, G.G. (2004). The BACK domain in BTB-kelch proteins. Trends Biochem Sci *29*,
1322 634–637.
1323 92. Akter, F., Bonini, S., Ponnaiyan, S., Kögler-Mohrbacher, B., Bleibaum, F., Damme, M., Renard, B.Y., and
1324 Winter, D. (2023). Multi–Cell Line Analysis of Lysosomal Proteomes Reveals Unique Features and Novel
1325 Lysosomal Proteins. Molecular & Cellular Proteomics *22*, 100509. 10.1016/j.mcpro.2023.100509.

93. Martinez-Val, A., Bekker-Jensen, D.B., Steigerwald, S., Koenig, C., Østergaard, O., Mehta, A., Tran, T., Sikorski, K., Torres-Vega, E., Kwasniewicz, E., et al. (2021). Spatial-proteomics reveals phospho-signaling dynamics at subcellular resolution. Nat Commun *12*. 10.1038/s41467-021-27398-y.
94. Szklarczyk, D., Kirsch, R., Koutrouli, M., Nastou, K., Mehryary, F., Hachilif, R., Gable, A.L., Fang, T., Doncheva, N.T., Pyysalo, S., et al. (2023). The STRING database in 2023: protein–protein association networks and functional enrichment analyses for any sequenced genome of interest. Nucleic Acids Res *51*, D638–D646. 10.1093/nar/gkac1000.
95. Oughtred, R., Rust, J., Chang, C., Breitkreutz, B.J., Stark, C., Willems, A., Boucher, L., Leung, G., Kolas, N., Zhang, F., et al. (2021). The BioGRID database: A comprehensive biomedical resource of curated protein, genetic, and chemical interactions. Protein Science *30*, 187–200. 10.1002/pro.3978.
96. Xiao, Q., Yan, P., Ma, X., Liu, H., Perez, R., Zhu, A., Gonzales, E., Burchett, J.M., Schuler, D.R., Cirrito, J.R., et al. (2014). Enhancing astrocytic lysosome biogenesis facilitates Aβ clearance and attenuates amyloid plaque pathogenesis. Journal of Neuroscience *34*, 9607–9620. 10.1523/JNEUROSCI.3788-13.2014.
97. Lee, J.H., Yang, D.S., Goulbourne, C.N., Im, E., Stavrides, P., Pensalfini, A., Chan, H., Bouchet-Marquis, C., Bleiwas, C., Berg, M.J., et al. (2022). Faulty autolysosome acidification in Alzheimer's disease mouse models induces autophagic build-up of Aβ in neurons, yielding senile plaques. Nat Neurosci *25*, 688–701. 10.1038/s41593-022-01084-8.
98. Zhang, W., Xu, C., Sun, J., Shen, H.M., Wang, J., and Yang, C. (2022). Impairment of the autophagy–lysosomal pathway in Alzheimer's diseases: Pathogenic mechanisms and therapeutic potential. Preprint at Chinese Academy of Medical Sciences, 10.1016/j.apsb.2022.01.008 10.1016/j.apsb.2022.01.008.
99. Mary, A., Eysert, F., Checler, F., and Chami, M. (2023). Mitophagy in Alzheimer's disease: Molecular defects and therapeutic approaches. Preprint at Springer Nature, 10.1038/s41380-022-01631-6 10.1038/s41380-022-01631-6.
100. Gowrishankar, S., Yuan, P., Wu, Y., Schrag, M., Paradise, S., Grutzendler, J., De Camilli, P., and Ferguson, S.M. (2015). Massive accumulation of luminal protease-deficient axonal lysosomes at Alzheimer's disease amyloid plaques. Proc Natl Acad Sci U S A *112*, E3699–E3708. 10.1073/pnas.1510329112.
101. Prasad, H., and Rao, R. (2018). Amyloid clearance defect in ApoE4 astrocytes is reversed by epigenetic correction of endosomal pH. Proc Natl Acad Sci U S A *115*, E6640–E6649. 10.1073/pnas.1801612115.
102. Park, H., Hundley, F. V., Yu, Q., Overmyer, K.A., Brademan, D.R., Serrano, L., Paulo, J.A., Paoli, J.C., Swarup, S., Coon, J.J., et al. (2022). Spatial snapshots of amyloid precursor protein intramembrane processing via early endosome proteomics. Nat Commun *13*. 10.1038/s41467-022-33881-x.
103. Morrow, J.A., Hatters, D.M., Lu, B., Höchtl, P., Oberg, K.A., Rupp, B., and Weisgraber, K.H. (2002). Apolipoprotein E4 forms a molten globule: A potential basis for its association with disease. Journal of Biological Chemistry *277*, 50380–50385. 10.1074/jbc.M204898200.
104. Zellner, A., Müller, S.A., Lindner, B., Beaufort, N., Rozemuller, A.J.M., Arzberger, T., Gassen, N.C., Lichtenthaler, S.F., Kuster, B., Haffner, C., et al. (2022). Proteomic profiling in cerebral amyloid angiopathy reveals an overlap with CADASIL highlighting accumulation of HTRA1 and its substrates. Acta Neuropathol Commun *10*. 10.1186/s40478-021-01303-6.
105. Dai, J., Johnson, E.C.B., Dammer, E.B., Duong, D.M., Gearing, M., Lah, J.J., Levey, A.I., Wingo, T.S., and Seyfried, N.T. (2018). Effects of APOE Genotype on Brain Proteomic Network and Cell Type Changes in Alzheimer's Disease. Front Mol Neurosci *11*. 10.3389/fnmol.2018.00454.
106. Johnson, E.C.B., Carter, E.K., Dammer, E.B., Duong, D.M., Gerasimov, E.S., Liu, Y., Liu, J., Betarbet, R., Ping, L., Yin, L., et al. (2022). Large-scale deep multi-layer analysis of Alzheimer's disease brain reveals strong proteomic disease-related changes not observed at the RNA level. Nat Neurosci *25*, 213–225. 10.1038/s41593-021-00999-y.
107. Askenazi, M., Kavanagh, T., Pires, G., Ueberheide, B., Wisniewski, T., and Drummond, E. (2023). Compilation of reported protein changes in the brain in Alzheimer's disease. Nat Commun *14*. 10.1038/s41467-023-40208-x.
108. Aber, R., Chan, W., Mugisha, S., and Jerome-Majewska, L.A. (2019). Transmembrane emp24 domain proteins in development and disease. Preprint at Cambridge University Press, 10.1017/S0016672319000090 10.1017/S0016672319000090.
109. Astillero-Lopez, V., Gonzalez-Rodriguez, M., Villar-Conde, S., Flores-Cuadrado, A., Martinez-Marcos, A., Ubeda-Banon, I., and Saiz-Sanchez, D. (2022). Neurodegeneration and astrogliosis in the entorhinal cortex in

1379 Alzheimer's disease: Stereological layer-specific assessment and proteomic analysis. Alzheimer's and Dementia *18*,
1380 2468–2480. 10.1002/alz.12580.
1381 110. Costa, J., Pronto-Laborinho, A., Pinto, S., Gromicho, M., Bonucci, S., Tranfield, E., Correia, C., Alexandre,
1382 B.M., and de Carvalho, M. (2020). Investigating LGALS3BP/90 K glycoprotein in the cerebrospinal fluid of patients
1383 with neurological diseases. Sci Rep *10*. 10.1038/s41598-020-62592-w.
1384 111. Seki, T., Kanagawa, M., Kobayashi, K., Kowa, H., Yahata, N., Maruyama, K., Iwata, N., Inoue, H., and
1385 Toda, T. (2020). Galectin 3– binding protein suppresses amyloid-β production by modulating β-cleavage of amyloid
1386 precursor protein. Journal of Biological Chemistry *295*, 3678–3691. 10.1074/jbc.RA119.008703.
1387 112. Zheng, J., Cao, Y., Yang, J., and Jiang, H. (2022). UBXD8 mediates mitochondria-associated degradation to
1388 restrain apoptosis and mitophagy. EMBO Rep *23*. 10.15252/embr.202254859.
1389 113. Batra, S., Vaquer-Alicea, J., Manon, V.A., Kashmer, O.M., Lemoff, A., Cairns, N.J., White, C.L., and
1390 Diamond, M.I. (2023). VCP increases or decreases tau seeding using specific cofactors. bioRxiv *2023.08.30.555637*.
1391 10.1101/2023.08.30.555637.
1392 114. Zeng, J., Shirihai, O.S., and Grinstaff, M.W. (2020). Modulating lysosomal pH: a molecular and nanoscale
1393 materials design perspective. JoLS, Journal of Life Sciences. 10.36069/jols/20201204.
1394 115. Li, H., Doric, Z., Berthet, A., Jorgens, D.M., Nguyen, M.K., Hsieh, I., Margulis, J., Fang, R., Debnath, J.,
1395 Sesaki, H., et al. (2021). Longitudinal tracking of neuronal mitochondria delineates PINK1/Parkin-dependent
1396 mechanisms of mitochondrial recycling and degradation. Sci Adv *7*. 10.1126/sciadv.abf6580.
1397 116. Falcón-Pérez, J.M., Nazarian, R., Sabatti, C., and Dell'Angelica, E.C. (2005). Distribution and dynamics of
1398 Lamp1-containing endocytic organelles in fibroblasts deficient in BLOC-3. J Cell Sci *118*, 5243–5255.
1399 10.1242/jcs.02633.
1400 117. Watts, J.A., Grunseich, C., Rodriguez, Y., Liu, Y., Li, D., Burdick, J.T., Bruzel, A., Crouch, R.J., Mahley,
1401 R.W., Wilson, S.H., et al. (2022). A common transcriptional mechanism involving R-loop and RNA abasic site
1402 regulates an enhancer RNA of APOE. Nucleic Acids Res *50*, 12497–12514. 10.1093/nar/gkac1107.
1403 118. Sun, N., Yun, J., Liu, J., Malide, D., Liu, C., Rovira, I.I., Holmström, K.M., Fergusson, M.M., Yoo, Y.H.,
1404 Combs, C.A., et al. (2015). Measuring In Vivo Mitophagy. Mol Cell *60*, 685–696. 10.1016/j.molcel.2015.10.009.
1405 119. Bouhaddou, M., Memon, D., Meyer, B., White, K.M., Rezelj, V. V., Correa Marrero, M., Polacco, B.J.,
1406 Melnyk, J.E., Ulferts, S., Kaake, R.M., et al. (2020). The Global Phosphorylation Landscape of SARS-CoV-2
1407 Infection. Cell *182*, 685-712.e19. 10.1016/j.cell.2020.06.034.
1408 120. Reilly, L., Lara, E., Ramos, D., Li, Z., Pantazis, C.B., Stadler, J., Santiana, M., Roberts, J., Faghri, F., Hao,
1409 Y., et al. (2023). A fully automated FAIMS-DIA mass spectrometry-based proteomic pipeline. Cell Reports Methods,
1410 100593. 10.1016/j.crmeth.2023.100593.
1411 121. Olivella, R., Chiva, C., Serret, M., Mancera, D., Cozzuto, L., Hermoso, A., Borràs, E., Espadas, G., Morales,
1412 J., Pastor, O., et al. (2021). QCloud2: An Improved Cloud-based Quality-Control System for Mass-Spectrometry-
1413 based Proteomics Laboratories. J Proteome Res *20*, 2010–2013. 10.1021/acs.jproteome.0c00853.
1414 122. Choi, M., Chang, C.Y., Clough, T., Broudy, D., Killeen, T., MacLean, B., and Vitek, O. (2014). MSstats:
1415 An R package for statistical analysis of quantitative mass spectrometry-based proteomic experiments. Bioinformatics
1416 *30*, 2524–2526. 10.1093/bioinformatics/btu305.
1417 123. Yu, G., Wang, L.G., Han, Y., and He, Q.Y. (2012). ClusterProfiler: An R package for comparing biological
1418 themes among gene clusters. OMICS *16*, 284–287. 10.1089/omi.2011.0118.
1419 124. Gu, Z., Eils, R., and Schlesner, M. (2016). Complex heatmaps reveal patterns and correlations in
1420 multidimensional genomic data. Bioinformatics *32*, 2847–2849. 10.1093/bioinformatics/btw313.
1421 125. Gu, Z. (2022). Complex heatmap visualization. iMeta *1*. 10.1002/imt2.43.
1422 126. Jurrus, E., Engel, D., Star, K., Monson, K., Brandi, J., Felberg, L.E., Brookes, D.H., Wilson, L., Chen, J.,
1423 Liles, K., et al. (2018). Improvements to the APBS biomolecular solvation software suite. Protein Science *27*, 112–
1424 128. 10.1002/pro.3280.
1425 127. Hodes, R.J., and Buckholtz, N. (2016). Accelerating Medicines Partnership: Alzheimers Disease (AMP-AD)
1426 Knowledge Portal Aids Alzheimers Drug Discovery through Open Data Sharing. Preprint at Taylor and Francis Ltd,
1427 10.1517/14728222.2016.1135132 10.1517/14728222.2016.1135132.
1428 128. Logsdon, B.A., Perumal, T.M., Swarup, V., Wang, M., Funk, C., Allen, M., Wang, X., Dammer, E.,
1429 Srivastava, G., Mukherjee, S., et al. (2019). Meta-analysis of the human brain transcriptome identifies heterogeneity
1430 across human AD 1 coexpression modules robust to sample collection and methodological approach 2 3. bioRxiv.
1431 https://doi.org/10.1101/510420.

1432 129. Seyfried, N.T., Dammer, E.B., Swarup, V., Nandakumar, D., Duong, D.M., Yin, L., Deng, Q., Nguyen, T.,
1433 Hales, C.M., Wingo, T., et al. (2017). A Multi-network Approach Identifies Protein-Specific Co-expression in
1434 Asymptomatic and Symptomatic Alzheimer's Disease. Cell Syst *4*, 60-72.e4. 10.1016/j.cels.2016.11.006.
1435 130. Zhang, B., and Horvath, S. (2005). A general framework for weighted gene co-expression network analysis.
1436 Stat Appl Genet Mol Biol *4*, 17. 10.2202/1544-6115.1128.
1437 131. Langfelder, P., and Horvath, S. (2007). Eigengene networks for studying the relationships between co-
1438 expression modules. BMC Syst Biol *1*, 54. 10.1186/1752-0509-1-54.
1439 132. Wilcoxon, F. (1945). Individual Comparisons by Ranking Methods. Biometrics Bulletin *1*, 80–83.
1440 133. Pearson, E.S. (1931). The Test of Significance for the Correlation Coefficient. J Am Stat Assoc *26*, 128–
1441 134. 10.1080/01621459.1931.10503208.
1442

Supplemental Figures

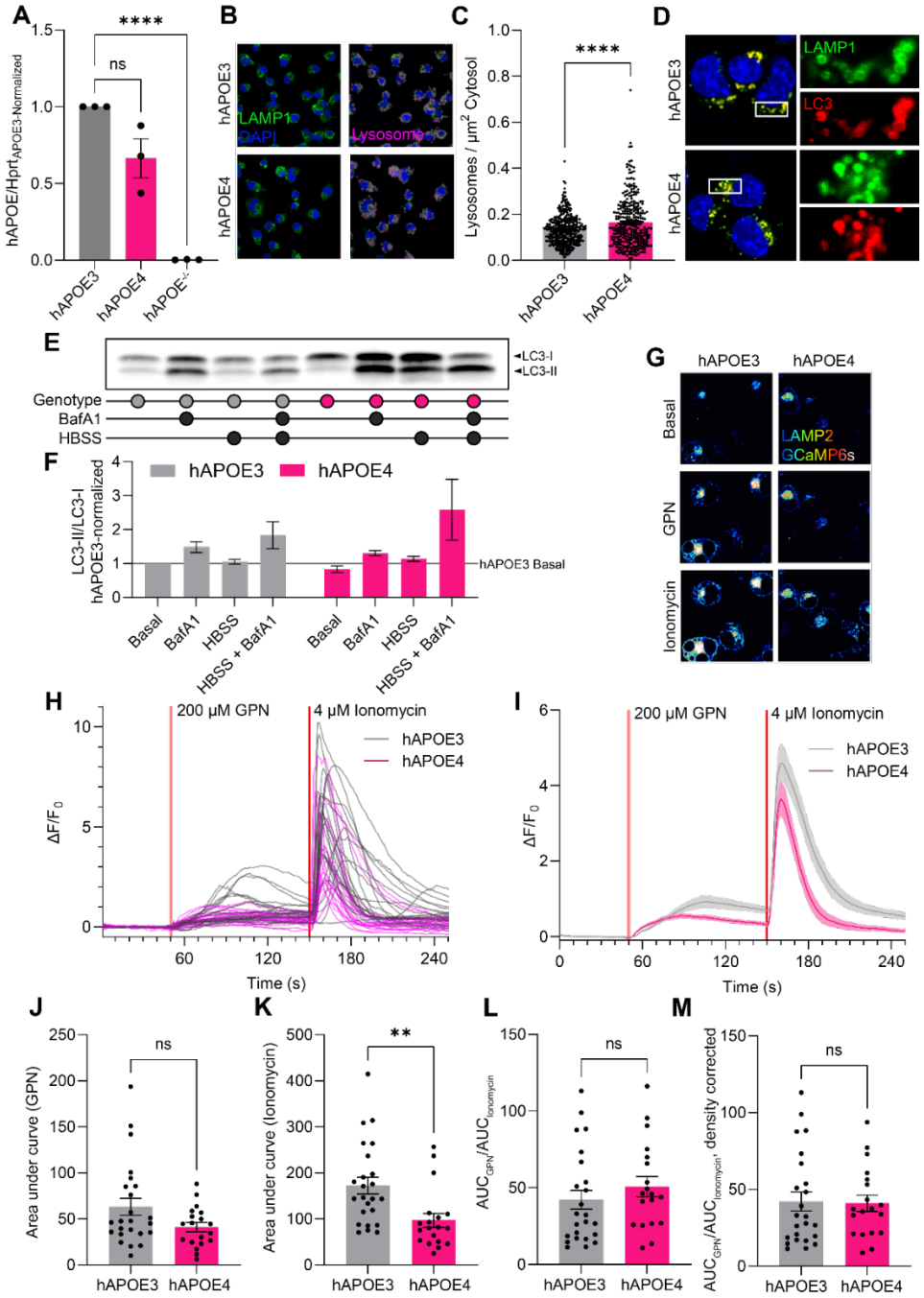

Figure S1: Lysosomal calcium content. (**A**) *hAPOE* gene expression across Neuro-2a cell lines, measured by RT-qPCR. (**B**) Immunofluorescence of Neuro-2a cells expressing hAPOE3 or hAPOE4, stained for the integral lysosomal membrane protein LAMP1. Right panels show puncta identification using Fiji. (**C**) Lysosomal density per cell based on images such as those in panel B. (**D**) Immunofluorescence of LAMP1 and LC3 shows lysosome-autophagosome fusion in both hAPOE3 and hAPOE4 Neuro-2a cells following 3 hours HBSS starvation and BafA1 treatment. (**E**) Representative western blot of LC3-I and LC3-II in hAPOE3 and hAPOE4 Neuro-2a cells. (**F**) Quantification of LC3-II/LC3-I ratio, normalized to internal hAPOE3 controls, across three independent replicates. (**G**) LAMP2-GCaMP6s lysosomal calcium measurements in Neuro-2a cells shown at basal states, and upon sequential stimulation using 200 µM GPN to release lysosomal calcium, and 4 µM Ionomycin to release total calcium. (**H**) Single-cell traces for lysosomal calcium release, as shown in panel D. (**I**) Mean traces of lysosomal calcium release, alongside SEM error bar traces. (**J**) Lysosomal calcium signals, as measured by the area under the curve following GPN and Ionomycin stimulation. (**K**) Total calcium sensitivity of apoE3 and apoE4 cells, as measured by the area under the curve following Ionomycin stimulation. (**L**) Relative lysosomal calcium release, normalized to the calcium sensitivity. (**M**) Relative lysosomal calcium release normalized to the lysosomal density, as calculated in panel C, estimates the lysosomal calcium content of each individual lysosome.

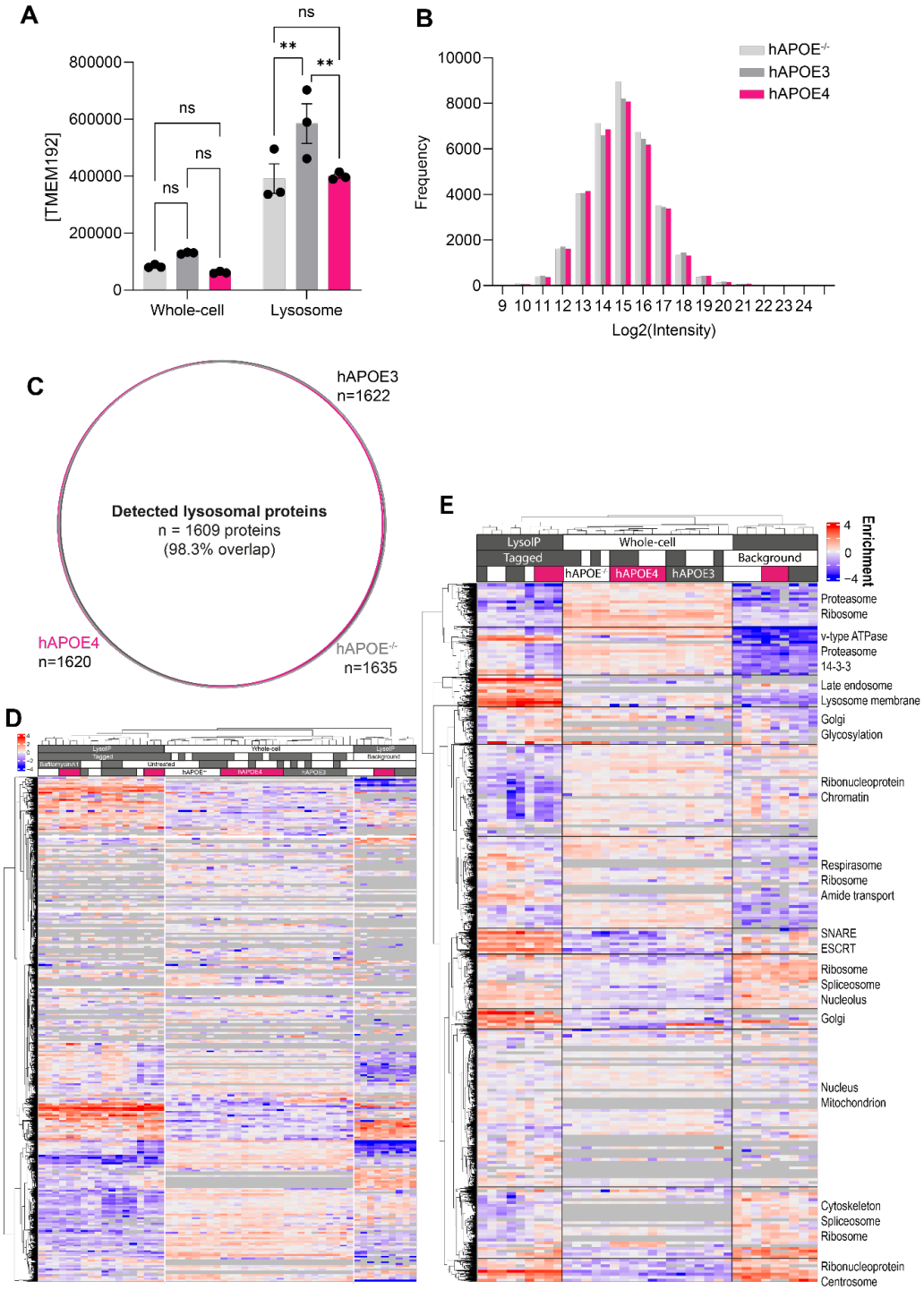

Figure S2: Abundance proteome coverage and clustering across apoE genotypes. (**A**) Human lysosomal TMEM192 tag intensities in whole-cell and lysosomal fractions of untreated Neuro-2a cells from 3 independent experiments. (**B**) Histogram of Log2-transformed protein group intensities across all obtained Neuro-2a lysosomal proteomes, stratified by genotype. (**C**) Venn diagram of lysosome-enriched proteins detected in LysoIP samples across genotypes. (**D**) Full heat-map generated from raw intensities of all detected proteins across all samples reveals distinct clustering of LysoIP, whole-cell, and LysoIP background datasets, as well as sub-clustering based on Bafilomycin treatment and apoE genotype. (**E**) Heat map excluding BafA1-treated samples, including cellular component annotations of detected proteins. Groups of data were analyzed in GraphPad Prism by 2-way ANOVA followed *post-hoc* by Dunnett's multiple comparisons test. **P<0.01.

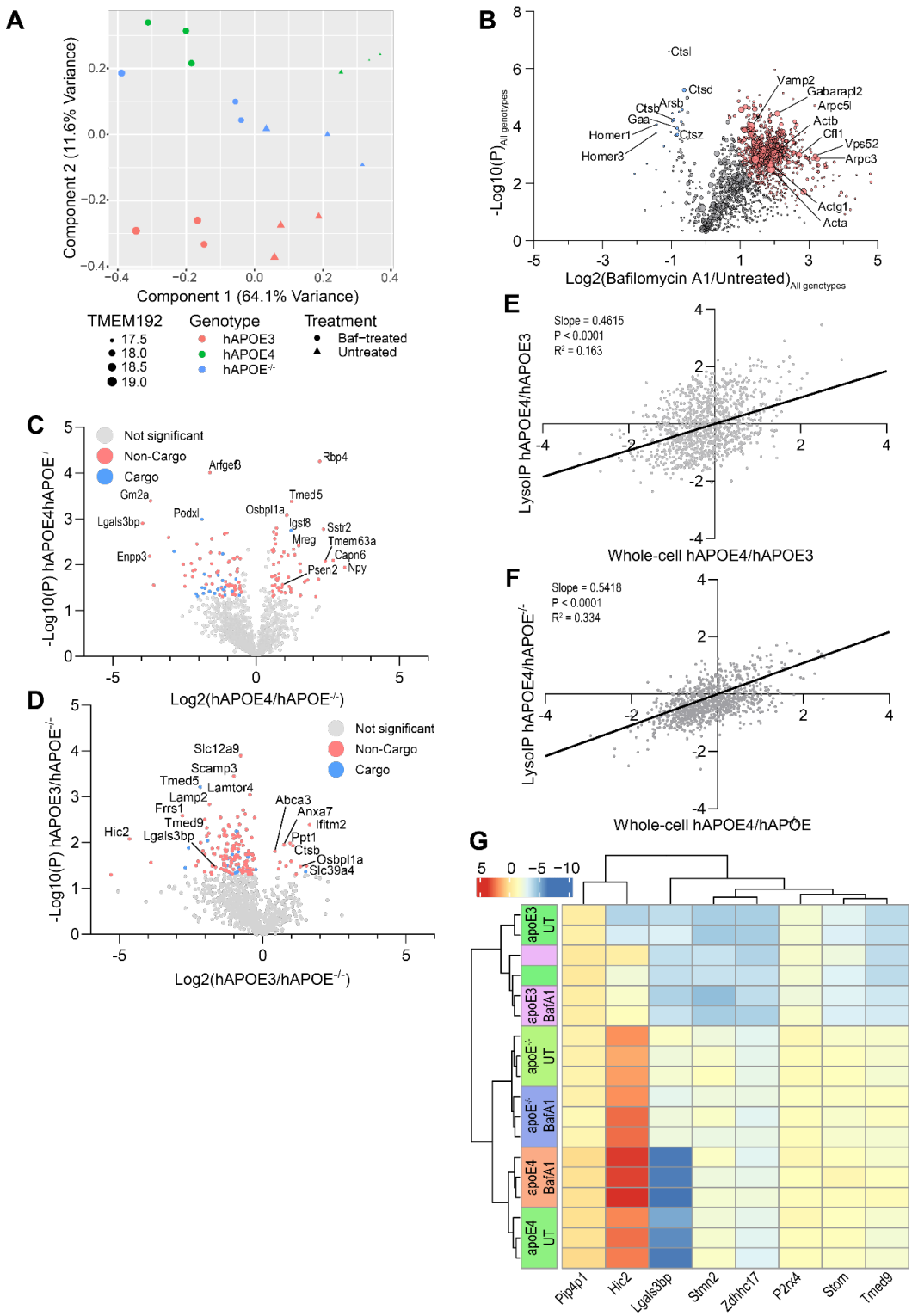

Figure S3: Proteomic comparisons of apoE lysosomes. (**A**) Principal component analysis of all lysosomal proteomes separates samples based on Bafilomycin treatment (component 1) and apoE genotype (component 2). (**B**) Volcano plot comparing BafA1 and untreated lysosomal proteomes, pooled across hAPOE genotypes. Node sizes indicate relative protein abundances following BafA1 treatment. (**C-D**) Volcano plot comparing hAPOE4 and hAPOE$^{-/-}$(C) or hAPOE3 and hAPOE$^{-/-}$ (D) lysosomal proteomes. Proteins significantly changed in hAPOE4 lysosomes are colored by their status as a lysosomal cargo protein, based on basal (red) or BafA1-dependent (blue) lysosomal enrichment. (**E-F**) Comparison of hAPOE4-associated changes to whole-cell and lysosomal protein abundances to hAPOE3 (E) and

hAPOE$^{-/-}$ (F) proteomes, showing positive correlation between changed whole-cell and lysosomal protein levels. Only proteins detected across four sample sets (genotype and fraction) were be plotted. (**G**) Partial least squares-discriminant analysis of lysosomal proteomes reveals proteins separating experimental groups. In particular, hAPOE4 was accompanied by lysosomal Lgals3bp depletion.

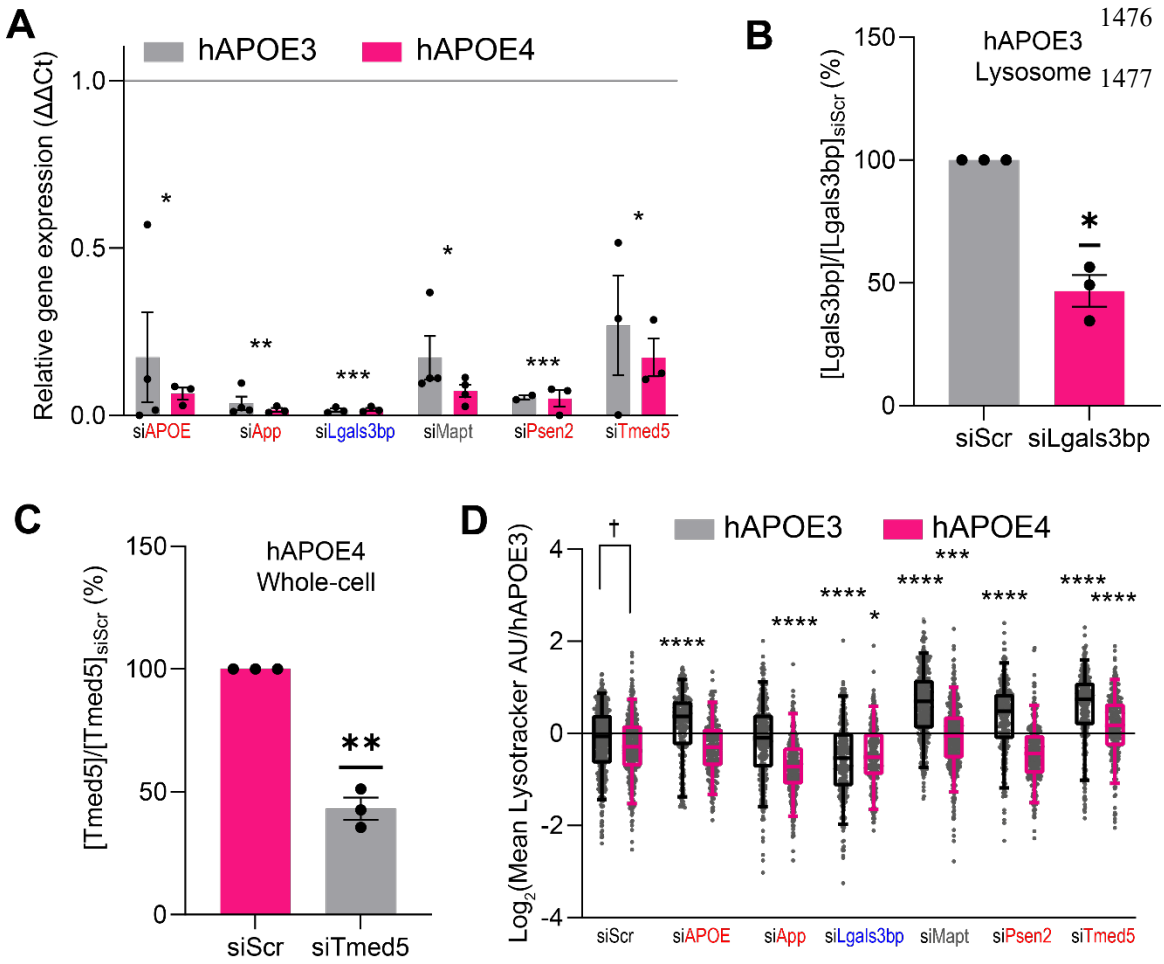

Figure S4: Identification of proteomic drivers underlying hAPOE4 lysosomal defects. (**A**) Gene expression upon targeting indicated genes with siRNAs in Neuro-2a cells. Expression level changes are indicated relative to *Hprt* expression and siScr-treated cells. (**B**) Efficiency of Lgals3bp protein reduction in hAPOE3 lysosomes upon Lgals3bp siRNA knockdown relative to scrambled siRNA controls as measured by mass spectrometry. Lysosomal Lgals3bp was measured since it was undetected in the whole-cell lysate upon knockdown, precluding calculation of its knockdown efficiency. (**C**) Efficiency of Tmed5 protein reduction in hAPOE4 whole-cell lysate upon Tmed5 siRNA knockdown relative to scrambled siRNA controls as measured by mass spectrometry. (**D**) Influence of gene silencing on LysoTracker staining, normalized to hAPOE3 LysoTracker intensity. Knockdown comparisons are performed relative to the same genotype siScr control. Dagger (†) comparison shows difference between hAPOE3 and hAPOE4 cells. Data points indicate individual cells from three independent experiments. Groups of data were analyzed in GraphPad Prism by 2-way ANOVA followed *post-hoc* by Dunnett's multiple comparisons test. Pairs of data were analyzed by t-tests. *P<0.05, **P<0.01, ***P<0.001, ****P<0.0001.

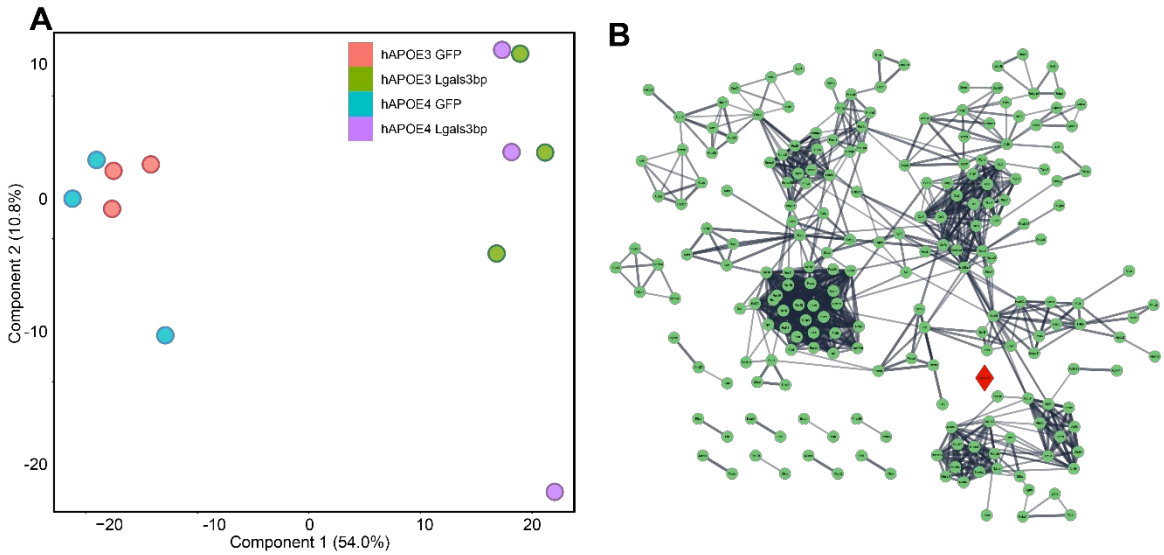

Figure S5: The neuronal Lgals3bp interactome. (**A**) Principal component analysis of affinity-purified proteomes shows clustering of Lgals3bp-GFP-purified samples distinct from GFP background samples (component 1), and slight separation of apoE3 and apoE4 samples (component 2). (**B**) Physical STRING subnetwork of identified Lgals3bp interactors. Lgals3bp is highlighted in red.

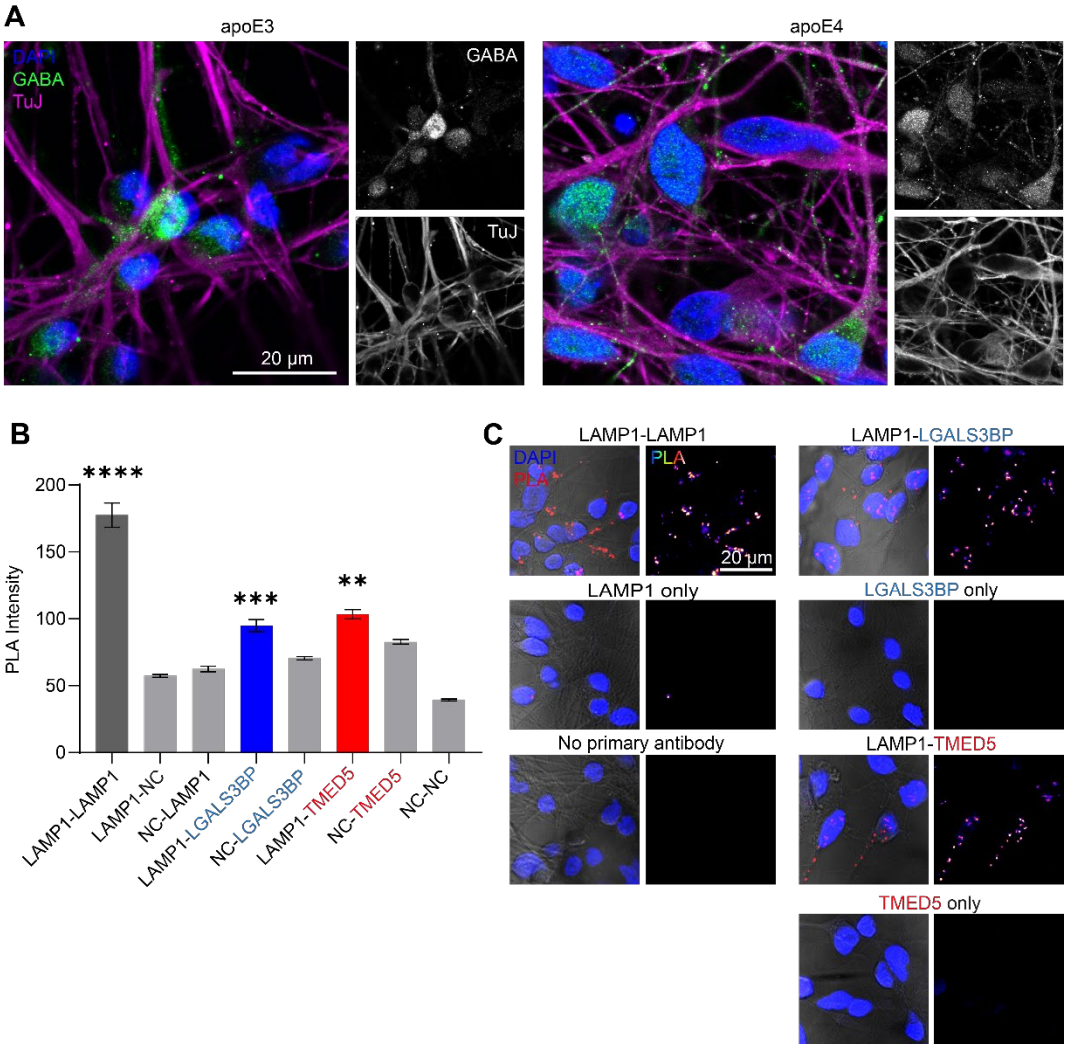

Figure S6: Controls for iPSC-derived neuron proximity ligation assay. (**A**) Immunofluorescence of neuronal markers following 49 days of differentiation, revealing pure cultures of TuJ^+ neurons including $GABA^+$ interneurons for both genotypes. (**B**) Establishing PLA sensitivities, showing significant signals above single antibody negative controls (NC) for LAMP1-LAMP1, LAMP1-LGALS3BP, and LAMP1-TMED5 assays. (**C**) Representative images for quantification shown in panel B. Individual cells from three independent experiments were analyzed by a one-way ANOVA followed by a *post-hoc* Bonferroni multiple comparison test between dual antibody samples and single-antibody controls; the least statistically significant comparison is highlighted. **P<0.01, ***P<0.001, ****P<0.0001.